SOURCE MECHANISM OF VOLCANIC EXPLOSIONS INVESTIGATED BY SEISMO-ACOUSTIC OBSERVATIONS

Keehoon Kim

A dissertation submitted to the faculty of the University of North Carolina at Chapel Hill in partial fulfillment of the requirements for the degree of Doctor of Philosophy in the Department of Geological Sciences.

Chapel Hill
2013

Approved by:

Dr. Jonathan M. Lees

Dr. Lara S. Wagner

Dr. Jose A. Rial

Dr. Kevin G. Stewart

Dr. Delwayne Bohnenstiehl

Abstract

KEEHOON KIM: Source Mechanism of Volcanic Explosions
Investigated by Seismo-Acoustic Observations
(Under the direction of Dr. Jonathan M. Lees)

Source mechanisms of explosive, volcanic eruptions are critical for understanding magmatic plumbing systems, determining the evolution and geometry of source regions, and assessing eruptive behavior as well as hazard impact. In the last two decades, volcano seismo-infrasonic observations have become an essential part of volcano monitoring systems. Because the open vent of a volcano is a corridor connecting the solid earth to the atmosphere, explosive eruptions efficiently excite both infrasound and seismic waves. Each of these mechanical waves includes characteristic information on several stages of the eruption process, and the coupling of these processes sheds considerable light into volcano dynamics. In this dissertation, details of the explosive eruption mechanism are investigated by seismo-acoustic observations at two volcanoes: Karymsky Volcano in Kamchatka, Russia, and Tungurahua Volcano, Ecuador. First, path effects of infrasound waves near volcanic craters are investigated as they pass the rim of the vent and propagate to remote stations. Next, characteristics of infrasonic sources excited by volcanic explosion are explored. Distortion due to diffraction and reflection of infrasound at the crater vent is shown to be significant and must be accounted for when interpreting explosion source physics from wave fields. To address these problems we propose an acoustic, multipole source model in a half-space for volcanic explosions. Acoustic observations at Tungurahua Volcano appear to corroborate this model. Finally, source mechanisms of explosive eruptions at Tungurahua are investigated by jointly analyzing infrasound and seismic waves.

Using this approach, the time evolution and geometric orientation of the magmatic plumbing system, during a period of volcanic crises at Tungurahua, are illuminated and explained.

Dedication

To my family, who supported me each step of my way.

Acknowledgements

I would like to thank Dr. Jonathan Lees for his guidance during my Ph. D. research. He has been an excellent mentor as well as a good friend. I also would like to thank all members of the seismology group in the Department of Geological Sciences at UNC for their kind advice and comments.

TABLE OF CONTENTS

LIST OF TABLES

LIST OF FIGURES

CHAPTER 1.

Infrasonic wavefields excited by volcanic explosions

1.1 Abstract

Numerical modeling of waveform diffractions along the rim of a volcano vent shows high correlation to observed explosion signals at Karymsky Volcano, Kamchatka, Russia. The finite difference modeling assumed a gaussian source time function and an axisymmetric geometry. A clear demonstration of the significant distortion of infrasonic wavefronts was caused by diffraction at the vent rim edge. Data collected at Karymsky in 1997 and 1998 were compared to synthetic waveforms and variations of vent geometry were determined via grid search. Karymsky exhibited a wide range of variation in infrasonic waveforms, well explained by the diffraction, and modeled as changing vent geometry. Rim diffraction of volcanic infrasound is shown to be significant and must be accounted for when interpreting source physics from acoustic observations.

1.2 Introduction

In the last 10 years infrasonic acoustic waves have played an increasingly important role in understanding vent dynamics during explosive activity at numerous volcanoes (Garces and McNutt, 1997; Johnson et al., 2003; Lees et al., 2004). Relative to seis-

mic recordings of volcanic explosions, infrasound has a simplified Green's function and can thus provide a direct measure of physical source dynamics in the vicinity of the volcanic vent. Signals in the infrasonic frequency band (< 20 Hz) (Wilson and Forbes, 1969; Kanamori et al., 1994) can have several sources, and explicit wave simulation is required to extract and separate source dynamics from propagation effects. Although infrasonic waves are not as affected by path effects at short source-receiver distances, the distorting effects of vent geometry and atmospheric perturbation must be considered and removed in order to understand the underlying source dynamics of individual explosions.

We focus here on the volcanic vent geometry and its effect on infrasonic waveforms generated near the source during volcanic eruptions. When in close proximity to a volcano source (< 10 Km) propagation paths can be approximated by straight lines and atmospheric refraction and reflection distortion are, for the most part, negligible (Johnson et al., 2006; Ripepe et al., 2007). Here we model infrasound wavefields passing through a volcanic vent with varying radii and compare them with observations from Karymsky volcano, Russia. Wavefront deformation through the vent and past the rim is shown to be considerable and in significant agreement with field observations. We attribute the wave distortion to diffraction at the edge of the vent.

1.3 Data Acquisition

Karymsky Volcano is a 1540-m andesitic cone located in the central portion of Kamchatka's main active arc in Russia. Seismo-acoustic data presented here were collected at Karymsky volcano during two field surveys in August 1997 and September 1998 (Johnson et al., 2003; Lees et al., 2004). In 1997 and 1998, Karymsky exhibited long periods of discrete Strombolian explosive activity with a repetitive explosions ranging from 5 to 20 events per hour, on average. Stations were instrumented with PASS-

CAL Reftek A-07 and A-08 dataloggers with 3-component broadband seismometers and microphones on the lower flanks of the volcano, at distances 1500 - 5000 m from the summit crater (Figure 1.1a). In 1998, a microphone equipped with the Larsen-Davis 2570 electret condenser was used with laboratory-calibrated single-pole corner frequency at 0.27 Hz (3 dB down) and nominal sensitivity of 48 mV/Pa (Johnson, 2007). In 1997, however, a different electret condenser-based microphone was deployed (Johnson et al., 2003; Ripepe et al., 2007). The 1997 microphone was found to be sensitive to changes in pressure rather than absolute pressure, so measures of the time-derivative of pressure are recorded in the field. The electret condenser microphone has a flat response function in the audible band (20 Hz - 20 KHz), however calibration and sensitivity below 20 Hz is unavailable at this time, so detailed deconvolution is not possible. Since the signal-to-noise ratio for both 1997 and 1998 data are high and observations are in such good agreement with synthetic modeling, we present results from the 1997 modeling as corroboration of our approach in spite of the lack of calibration.

Among thousands of events recorded, 214 explosions (134 from 1997 and 80 from 1998) were selected for comparison to synthetic wave propagation modeling. Criteria for selection included: (1) impulsive, short duration signals (< 10 s) and (2) high signal-to-noise ratio (28 ± 9 dB) below 10 Hz. We thus avoid signals whose waveforms potentially interact with conduit walls and the fluid/air interface.

1.4 FDTD propagation model

A Finite-Difference Time-Domain (FDTD) method was used to synthesize acoustic wave propagation formulated as a set of first-order, velocity-pressure coupled differential equations (Ostashev et al., 2005). FDTD methods are powerful numerical tools widely used to study wave propagation in heterogeneous media including the

atmosphere and the ground (de Groot-Hedlin, 2008). To approximate the derivatives in the acoustic wave equation with finite differences, a staggered difference algorithm (Yee, 1966) was used in a two-dimensional cylindrical spatial domain. Time marching was staggered between the computations of pressure and particle velocity in the time domain. By restricting the computation to an axisymmetric cylindrical representation (volcanic cone and vent) calculations can be performed quickly on a desktop computer.

The perfectly matched layer technique (Berenger, 1994; Liu, 1999) was adapted for absorbing boundary conditions achieving highly effective suppression of reflections at the domain boundaries. In order to examine effects of ground surface and topographic reflections, diffractions, and scattering by the volcano geometry, a rigid boundary condition between the air and solid surface was implemented via the method of images (Morse and Ingard, 1986). Intrinsic attenuation and moving media are ignored in this simulation. In order to reduce numerical errors arising from the "staircase" representation of the rigid boundary, the model is spatially discretized using 20 grid points per wavelength, double the recommended minimum of 10 (Wang, 1996).

The volcanic conduit was modeled as an air-filled cylinder buried in a rigid volcanic cone, where the atmosphere was treated as a fluid halfspace connected to the magmatic system through the open vent (Figure 1.1b). In real volcanic environments, the conduit is likely filled with multi-phase fluids consisting of air, gas, and magma. In this study we simply assume that the top of the conduit consists of constant 340 m/s velocity air. Inhomogeneities and wind in the atmosphere, nonlinear behavior, and the effects of gravity are ignored. Supersonic flux of the initial mass and very large pressure purtubations ($> 10^3 Pa$) can cause non-linear shock waves. Strombolian ejection velocities, however, generally range up to a few hundred meters per second (Sparks, 1997). Source pressures calculated from Karymsky data do not exceed $10^2 Pa$, using point source assumptions (Johnson, 2003), so we have adopted the

linearized acoustic equation. Because our aim is to investigate deformation of wavefronts passing through the vent, longitudinal reflection at the air-magma interface is suppressed by incorporating an absorbing boundary at this interface, preventing down-going waves from being reflected back towards the summit.

The average outer radius of the active crater remained mostly constant at 45 meters from 1996 to 1998 based on geodetic observations (Alexei Ozerov, personal contact). Inner vent radius, depth and source frequency were allowed to vary as model parameters (Table 1.1).

The direct source of volcanic infrasound is atmospheric vibration at the air-magma interface. This perturbation can be generated by mass outflux through, or accelerating movement of, the interface. We use mass outflux here as the source because we have observed, visually, gas emission associated with infrasonic events. High amplitude infrasound is more effectively excited by explosive gas emission than by large displacement of the air-magma interface (Johnson et al., 2004). Mass flux is assumed here to be spatially constant over the air-magma interface, exciting only the plane wave mode in the conduit. The plane wave condition is not exact, as real volcanic sources most probably simultaneously excite radial modes. The conduit walls act as waveguides, however, preventing the low frequency radial modes from being generated. Therefore, the plane wave is the predominant mode in the conduit as long as the vent radial dimension is smaller than the source wavelength. A gaussian-shaped pulse (Blackman-Harris window function) was used as the source-time-function for the mass flux (Figure 1.2c).

1.5 Results

We first present modeling results from a vent with varying radii to compare with analytic solutions and to provide insight into diffraction effects at the edge of the

Table 1.1: Modeling Parameters illustrated in Figure 1.1b

Parameters	Values
Acoustic velocity for air	340 m/s
Density for air	1 kg/m^3
Source-time duration (T)	0.1 s - 2 s
Radius of vent (r)	1 m - 45 m
Depth of crater (d)	0 m - 80 m
Radius of crater (R)	45 m
Slope of volcanic flank (β)	30 °

vent. Sound propagation excited by a vibrating piston buried in the rigid halfspace has been widely studied in the field of acoustics (Harris, 1981). Briefly, acoustic wavefronts of overpressure from a vibrating piston are composed of two components: a plane "direct wave" generated by vertical piston movement propagating along the conduit axis, followed by spherical, "edge waves", produced by diffraction along the vent edge (Figure 1.2a). In the cylindrical region immediately above the vent, the consequent wavefront consists of a direct wave followed by edge waves. Outside the cylindrical region, however, two edge waves with opposite polarities are the major contributors to the wavefield (Weight and Hayman, 1978).

In most exploding volcano situations, for reasons of safety, receivers are restricted to flanks away from the vent rim, and edge effects contribute considerably to observed signals. If the source is impulsive (Figure 1.2c), the two inverted pulses are readily observed on real recordings (Figure 1.2d). The lag and amplitudes of the two inverted pulses are constrained by the conduit radius, assuming the radius is constant with depth. In our modeling domain, however, acoustic waves are affected by diffraction from the edge of the inner and outer apertures of the crater. In Figure 1.2a and 1.2b, two diffractions are illustrated. When the original waves emanate from the inner vent, they diffract and the diffracted waves oscillate horizontally inside the crater, generating multiple reflected waves. Thus, where the vent radius increases, the original waves are distorted in a complex way governed by both inner and outer

vent radii and the associated crater depth.

Figure 1.3 shows a series of transient acoustic waveforms deformed by different geometries and different source-time-functions. The waveform distortion from the two edge waves with opposite polarities is clear, and sensitive to the geometry of the vent. These synthetic waveforms were compared to real data observed at Karymsky and the fit is extremely good (> 0.83 cross-correlation values for 90% of events). One series of observations which illustrate the waveform dependency on the vent geometry and the source time duration is illustrated in Figure 1.3. Impulsive explosions and subsequent oscillations were successfully reproduced by numerical modeling. Numerical modeling indicates that diffraction at the vent edge plays a significant role in the observed waveforms.

1.6 Discussion and Conclusion

Based on the theory of acoustic radiation from a vibrating piston, the contribution of diffracted edge waves to the wavefield depends on the vibration velocity and the diameter of the piston. If the wavelength of the vibration is much larger than the piston diameter, the larger of the two edge waves overlaps such that the radiating pressure waves are proportional to the time derivative of the vibration velocity, i.e. the acceleration. In this limit, the piston corresponds to a point source radiator. On the other hand, if the velocity wavelength is shorter than the piston diameter, two edge waves can be resolved without overlap. In this case, each edge wave closely resembles (slightly dispersed) the vibration velocity rather than the acceleration (Weight and Hayman, 1978). Infrasound data recorded in the field at Karymsky exhibit this diffraction phenomenon. When the source wave length (265 m) is larger than the outer crater diameter (90 m), the observed waveform reduces to the time derivative of the source function (top panel, figure 1.3a). The duration of the pressure purturbation

is almost the same as that of the source time function representing mass flux. When the source wavelength (64 m) is shorter than the crater, however, the two edge waves can be separated such that the first arrived edge wave is highly correlated to the mass flux function (bottom panel, figure 1.3a) . The latter edge wave is more attenuated and may be contaminated by reverberations within the crater. This dependency on vent dimensions and source wavelength was observed also in 1997 (figure 1.3b) where the instrument recorded the time-derivative pressure field (Ripepe et al., 2007).

The assumption of a gaussian shaped source function and plane waves appears to be justified by the excellent correlation of model results with field observations. First, because only short duration pulses were selected from the Karymsky data, sources must be simple. Second, the vent wall behaves as a waveguide and the plane wave dominates even though the source wavelength is slightly shorter than or equal to the vent diameter. Third, the real source may have a vertical component amplitude larger than the radial component. The true directivity of the source can not be estimated without observations of the direct wave (as defined previously) above the vent or refracted in the far field.

We focused here primarily on the presence of edge waves near a volcanic crater and on how they are related to source waveforms. A more detailed study may provide insight to the relation of the time lag (Δt) between edge waves and the vent geometry, although that is beyond the scope of this paper. The time lag has a strong dependence on the source waveform and vent geometry, however, if the pulse wavelength is shorter than the vent diameter (bottom, figure 1.3a), the two edge waves do not overlap and the time lag can be reduced to a function of geometric parameters alone. In the case of a simple piston with constant radius, this time lag corresponds only to the piston diameter (Weight and Hayman, 1978). However, in our model with varying radii, the time lag depends on the inner vent radius and the depth as well as the outer crater radius. High frequency pulses thus play a critical role for delineating detailed

geometric features of the vent.

FDTD modelings of infrasonic observations from Karymsky volcano showed that the wavefields in the near field are significantly affected by diffraction. The morphology of the crater plays an essential role in waveform distortion. Our results show that it is critical to take diffraction effects into account when interpreting source physics of volcanic explosions from acoustic observations.

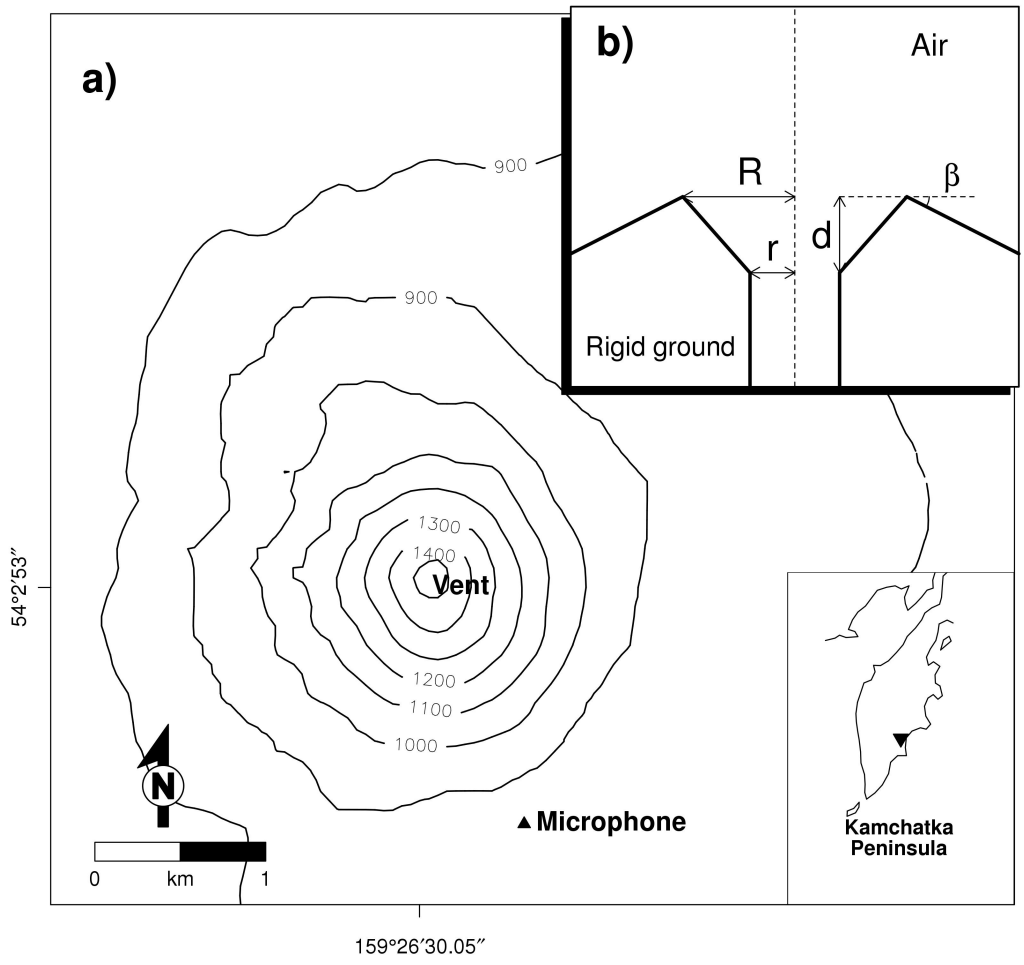

Figure 1.1: (a) Map of Karymsky volcano showing the microphone position during the two field experiments. (b) Cross-sectional view of the modeling domain illustrating the parameters and geometry of the model. Values of the parameters are listed in Table 1.1.

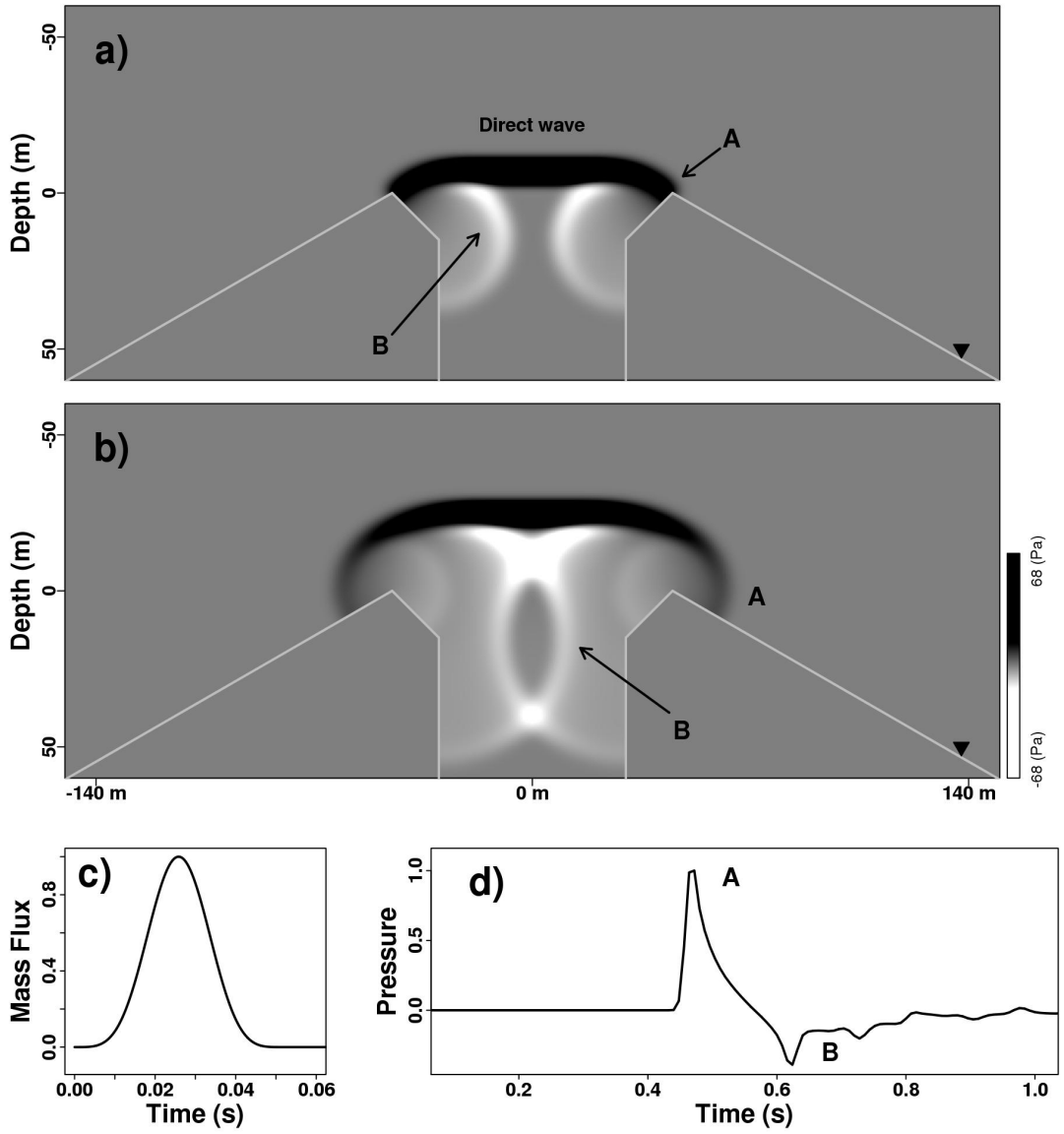

Figure 1.2: Modeling results that illustrate diffraction effects at the edge of the vent. The mass flux and pressure are normalized to the maximum value. (a) Snapshot of wavefronts diffracted from inner vent corner. Two edge waves with opposite polarities are indicated at A (positive) and B (negative). (b) Snapshot showing diffraction from outer crater rim. (c) Blackman-Harris function which has a 3dB cutoff frequency at 1/(time duration) Hz (d) Synthetic acoustogram recorded at the receiver (inverted triangle in Figure 1.1a). Peaks of the two edge waves (A and B) are clearly evident.

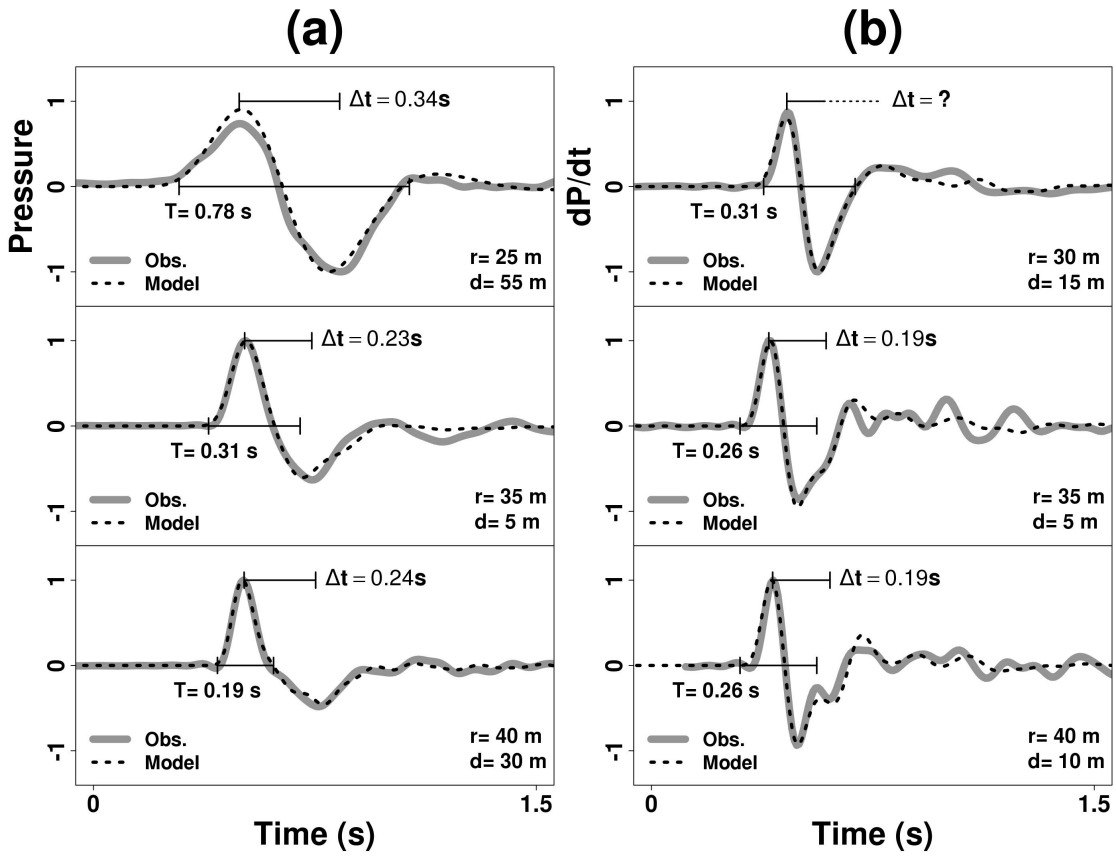

Figure 1.3: Comparison between model results and observations from Karymsky. The synthetic and observed signals are filtered by a low-pass filter ($\sim$ 10 Hz) and normalized to the maximum value. Modeling parameters are presented for each figure, where T = source-time duration, r = radius of inner vent and d = depth of crater, Δt = time lag between two inverted pulses attributed to overlapiping of edge waves. (a) Synthetic waves are modeled by gaussian source-time functions with different durations listed on the figure. Accompanying observations are from the 1998 experiments. (b) Comparison between synthetic waveforms and 1997 observations, where the rate of change of overpressure was modeled. The latter arriving edge wave is indistinguishable from the first because they overlap smoothly (top panel).

CHAPTER 2.

Volcanic infrasound source model

2.1 Abstract

Volcanic explosions are accompanied by strong acoustic pressure disturbances in the atmosphere. With a proper source model, these acoustic signals provide invaluable information about volcanic explosion dynamics. Far-field solutions to volcanic infrasound radiation have been derived above a rigid half-space boundary, and a simple inversion method was developed based on the half-space model. Acoustic monopole and dipole sources were estimated simultaneously from infrasound waveforms. Stability of the inversion procedure was assessed in terms of variances of source parameters, and the procedure was reliable with at least three stations around the infrasound source. Application of this method to infrasound observations recorded at Tungurahua volcano in Ecuador successfully produced a reasonable range of source parameters with acceptable variances. Observed strong directivity of infrasound radiation from explosions at Tungurahua are successfully explained by the directivity of a dipole source model. The resultant dipole axis, in turn, shows good agreement with the opening direction of the vent at Tungurahua which is considered to be the origin of the dipole source. The method is general and can be utilized to study any monopole, dipole, or combined sources generated by explosions.

2.2 Introduction

Volcanic eruptions are efficient sources of atmospheric pressure perturbations within the infrasound band (<20 Hz). Volcanic infrasound is a direct measurement of fluctuation at the magma-air interface, and the atmosphere in the vicinity of the vent has a relatively simple Green's function compared to the solid medium through which seismic waves propagate. Hence, volcanic infrasound can carry valuable information about source dynamics without significant loss of source features compared to the seismic counterpart (Vergniolle et al., 1996; Garces and McNutt, 1997; Ozerov et al., 2003; Johnson and Lees, 2010).

A proper acoustic source model is necessary to extract the underlying physics of volcanic eruptions from infrasound observations. Real acoustic sources producing volcanic infrasound have finite dimensions such as radius of bubble or vent. In this case, source geometry and frequency dependent diffraction must be considered (Kim and Lees, 2011). However, if the source region is compact with respect to the wavelength, then the source can be dealt with as a point with magnitude but no spatial dimension. This point source approximation has been widely used in volcanic infrasound studies to quantify acoustic energy produced during volcanic eruptions (Johnson et al., 2004; Johnson, 2007; Ripepe et al., 2007; Vergniolle et al., 2004).

A monopole is the simplest and most efficient point source of volcanic infrasound. Sound generated by a monopole radiates uniformly into all directions. Isotropic mass outflux during volcanic eruptions can be modeled as a monopole source, and volume or velocity of ejecting material can be estimated from acoustic pressure (Woulff and McGetchin, 1976; Johnson et al., 2004).

Forces generated during volcanic activity can be simulated by a dipole source, which has two successive monopoles out of phase by 180°. Pressure disturbance by a dipole source exhibits directivity in the radiation pattern, which depends on the

angle between the direction of the dipole and station location. Caplan-Auerbach et al. (2010) used acoustic power observed at Augustine volcano, Alaska, to estimate the velocity of material exiting the vent based on the dipole model.

In both cases, selecting a proper source model is critical for estimating energy flux in the vicinity of a volcanic vent. Most studies of volcanic infrasound have used either a monopole or dipole source exclusively to model acoustic sources of volcanic eruptions, but theoretically both types of acoustic sources can be excited simultaneously. For instance, an unbaffled loudspeaker is theoretically an ideal dipole source. However, sound measurements from the loudspeaker are not explained solely by the dipole model, and the substantial monopole component is also required (Li et al., 1997). Hence, "multipole" sources can be appropriate for acoustic sources of volcanic infrasound.

In this paper we review the solutions to the scalar wave equation for monopole and dipole sources in a half-space, and then present an inversion method based on the half-space model to estimate source parameters for a monopole and dipole simultaneously. The inversion method is applied to infrasound observations from Tungurahua volcano, Ecuador in 2010 which exhibited remarkable directivity in acoustic radiation. The inversion process successfully estimated stable and consistent source parameters corresponding to the recorded radiation patterns. Consequently, the infrasound radiation pattern observed at Tungurahua volcano is well explained by the multipole source. The dipole component contributes to the observed directivity, and the monopole does to the overall pressure level. The multipole source model in a half-space gives us a powerful method to cope with complicated sources for volcanic infrasound and to understand underlying source physics of volcanic eruptions.

2.3 Monopole and dipole source models in a free-space

Acoustic radiation fields from sources of limited spatial extent can be described in terms of a multipole series. If the source is acoustically compact, so that its largest dimension is much shorter than a wavelength, the multipole series converges rapidly and the first few terms remain nonzero. Consequently, compact sources are typically approximated as monopole, dipole, and quadrupole terms (Rossing, 2007) although only monopole and dipole cases are considered in this paper. It is convenient to write the total sound field in terms of a Green's function. Assuming a point source placed at $\mathbf{r_0} = (x_0, y_0, z_0)$ in an unbounded atmosphere, the total sound field $p(\mathbf{r}, t)$ satisfies the inhomogeneous wave equation

$$\nabla^2 p - \frac{1}{c^2}\frac{\partial^2 p}{\partial t^2} = -\delta(t)\delta(\mathbf{r} - \mathbf{r_0}), \tag{2.1}$$

where p is pressure, c is the sound speed, and $\mathbf{r} = (\mathbf{x}, \mathbf{y}, \mathbf{z})$ is a receiver position. If the source is simple-harmonic, so that $\delta(t)$ from the origin can be substituted by $e^{-i\omega t}$ the resulting wave motion is $p = \hat{p}(\omega)e^{-i\omega t}$, which satisfies the inhomogeneous Helmholtz equation

$$\nabla^2 \hat{p}(\omega) + k^2 \hat{p}(\omega) = -\delta(\mathbf{r} - \mathbf{r_0}). \tag{2.2}$$

The Green's function solution to the Helmholtz equation (Morse and Ingard, 1986) is

$$G_\omega(\mathbf{r}|\mathbf{r_0}) = \frac{1}{4\pi R} e^{ikR}, \tag{2.3}$$

where $R = |\mathbf{r} - \mathbf{r_0}|$. Because this is a solution only for a single frequency, the transient solution in the time domain must be obtained from integration with respect to all

frequencies, as follows:

$$\begin{aligned} G(\mathbf{r}, t|\mathbf{r_0}, t_0 = 0) &= \int_{-\infty}^{\infty} G_\omega(\mathbf{r}|\mathbf{r_0}) e^{-i\omega t} d\omega \\ &= \int_{-\infty}^{\infty} \frac{1}{4\pi R} e^{-i\omega(t-R/c)} d\omega \\ &= \frac{\delta(t - R/c)}{4\pi R}. \end{aligned} \tag{2.4}$$

$G(\mathbf{r}, t|\mathbf{r_0}, t_0)$ is the Green's function for Eq. (2.1), and $G_\omega(\mathbf{r}|\mathbf{r_0})$ can be interpreted as the Fourier transform pair of $G(\mathbf{r}, t|\mathbf{r_0}, t_0)$. Expressions for monopole and dipole sources can be derived subsequently from the Green's function.

2.3.1 Monopole source

A point monopole is the simplest source for sound (Fig. 2.1a). Consider the radiation from a pulsating sphere with a small radius. If the mass flow of fluid from the source is $S(t)$, which is called the monopole strength hereafter, the excess pressure radiated from a monopole can be expressed as (Morse and Ingard, 1986)

$$\nabla^2 p - \frac{1}{c^2} \frac{\partial^2 p}{\partial t^2} = -\dot{S}(t)\delta(\mathbf{r} - \mathbf{r_0}), \tag{2.5}$$

where $\dot{S}(t)$ is the mass flow rate per unit time, or mass acceleration in units of $\rho m^3/s^2$ where ρ is the fluid density in kg/m^3. If the source is harmonic such as $S(t) = \hat{S}(\omega)e^{-i\omega t}$, the solution can be expressed in terms of the Green's function (Eq. 2.3)

$$\begin{aligned} \hat{p}(\omega) &= -ikc\hat{S}(\omega)G_\omega \\ &= -\frac{ikc\hat{S}(\omega)}{4\pi R} e^{ikR}. \end{aligned} \tag{2.6}$$

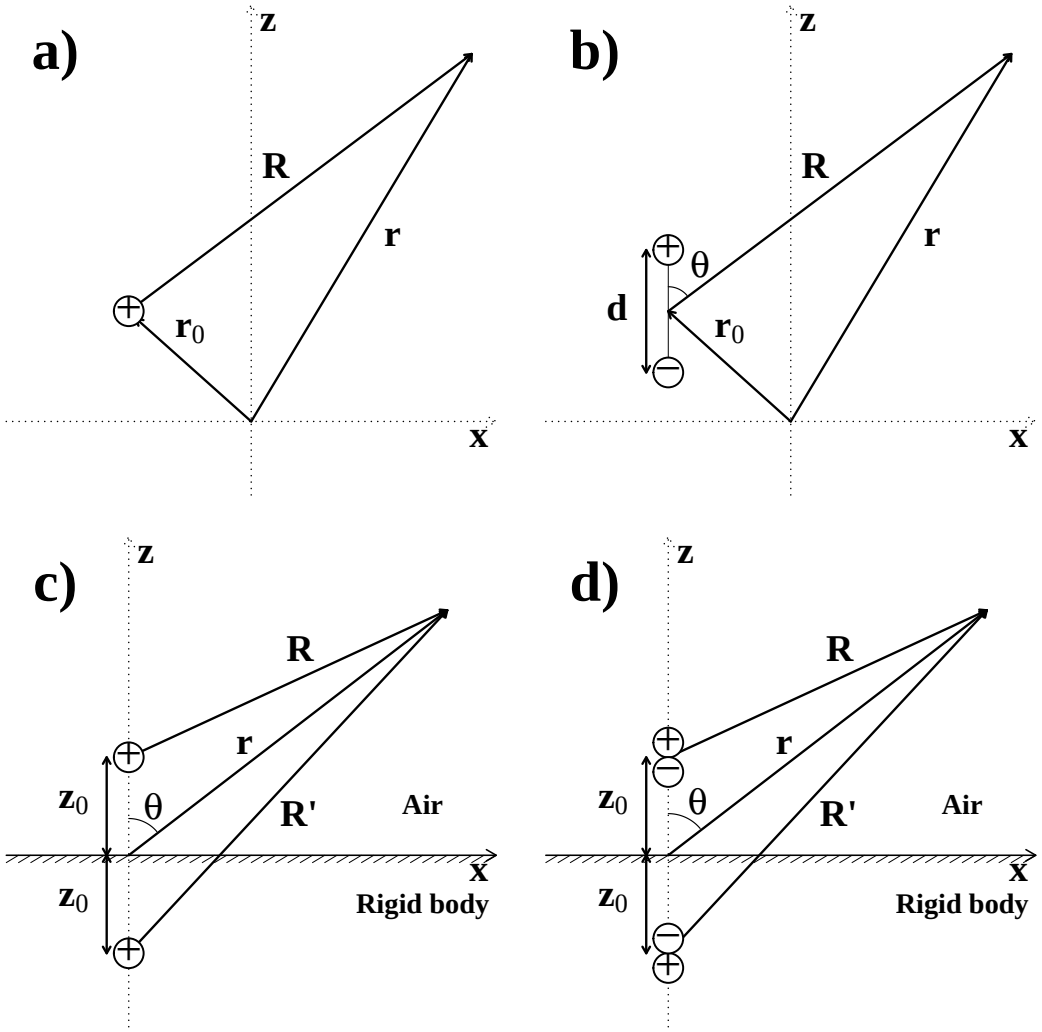

Figure 2.1: Geometric configurations for a) monopole in a free-space, where $\mathbf{r_0}$ and $\mathbf{r}$ are source and receiver positions, and $\mathbf{R}$ is the distance between the source and the receiver. b) dipole in a free-space, where $\mathbf{d}$ is the distance between two opposite point sources. c) monopole in a half-space, where $\mathbf{z_0}$ is the distance between a source and a half-space, and $\mathbf{R}'$ is the distance from the image of the source to a receiver. d) dipole in a half-space

The transient solution becomes

$$\begin{aligned} p(\mathbf{r},t) &= \int_{-\infty}^{\infty} \hat{p}(\omega) e^{-i\omega t} d\omega \\ &= \frac{1}{4\pi R} \dot{S}(t - \frac{R}{c}). \end{aligned} \tag{2.7}$$

The pressure at any point $\mathbf{r}$ in the field is omni-directional and determined by the mass acceleration $\dot{S}(t)$ of the simple source. A body of oscillating volume, such as a boxed loudspeaker at low frequencies, is a good example of a monopole source.

2.3.2 Dipole source

In order to generate the sound field from a point monopole, fluid must be introduced or withdrawn from a small region of space. In the dipole case sound can be produced by moving a portion of the fluid back and forth with no net introduction of fluid. The dipole source is simulated by a neighbouring pair of equal point monopoles with opposite signs. In this way fluid is being "breathed in" by one source as it is being "breathed out" by the other source. If the source of strength $S(t)$ is at $\mathbf{r_0} + \frac{1}{2}\mathbf{d}$ and the one of strength $-S(t)$ is at $\mathbf{r_0} - \frac{1}{2}\mathbf{d}$, and the vector distance ($\mathbf{d}$) between the two sources (Fig. 2.1b) is very small compared with the wavelength, then the wave equation for the dipole source can be expressed as (Morse and Ingard, 1986)

$$\begin{aligned} \nabla^2 p - \frac{1}{c^2}\frac{\partial^2 p}{\partial t^2} &= \nabla \cdot [\dot{S}(t)\mathbf{d}\,\delta(\mathbf{r} - \mathbf{r_0})] \\ &= -\dot{\mathbf{D}}(t) \cdot \nabla_0 \delta(\mathbf{r} - \mathbf{r_0}). \end{aligned} \tag{2.8}$$

$\mathbf{D}(t) \equiv S(t)\mathbf{d}$ is momentum in units of $kg \cdot m/s$, and the operator ∇_0 denotes the gradient with respect to the source coordinates, $\mathbf{r_0}$. Provided a harmonic source,

$\mathbf{D}(t) = \hat{\mathbf{D}}(\omega)e^{-i\omega t}$,

$$\begin{aligned}\hat{p}(\omega) &= -ikc\hat{\mathbf{D}}(\omega)\cdot\nabla_0 G_\omega(\mathbf{r}|\mathbf{r_0}) \\ &= -\frac{k^2c}{4\pi R}\left[1+\frac{i}{kR}\right]e^{ikR}\times\left[\frac{(x-x_0)}{R}\hat{D}_x+\frac{(y-y_0)}{R}\hat{D}_y+\frac{(z-z_0)}{R}\hat{D}_z\right] \quad (2.9)\end{aligned}$$

In the far field where the distance is much longer than the wavelength, the condition, $kR \gg 1$, is satisfied. Furthermore, if $\mathbf{r_0} = 0$ so that $|\mathbf{r}| = R = r$, equation (2.9) can be approximated as

$$\begin{aligned}\hat{p}(\omega) &\simeq -\frac{k^2c}{4\pi r}\left[\frac{x}{r}\hat{D}_x+\frac{y}{r}\hat{D}_y+\frac{z}{r}\hat{D}_z\right]e^{ikR} \quad (2.10)\\ &= -\frac{k^2c}{4\pi r}|\mathbf{D}_\omega|\cos\theta e^{ikR}, \quad (2.11)\end{aligned}$$

where θ is the angle between the dipole vector and the z coordinate axis (Fig. 2.1b). The sound field generated by the dipole shows directivity which depends on the angle θ. The magnitude of the pressure disturbances is maximum on the dipole axis, and zero at 90°. This dipole solution can be separated into two components: the vertical and horizontal. Any arbitrary dipole can be decomposed into vertical and horizontal dipoles and the sound field can be rewritten, as follows:

$$\hat{p}_{_H}(\omega) = -\frac{k^2c}{4\pi r}\left[\frac{x}{r}\hat{D}_x+\frac{y}{r}\hat{D}_y\right]e^{ikR}, \quad (2.12)$$

$$\hat{p}_{_V}(\omega) = -\frac{k^2c}{4\pi r}\left[\frac{z}{r}\hat{D}_z\right]e^{ikR}, \quad (2.13)$$

where $\hat{p}_{_H}(\omega)$ and $\hat{p}_{_V}(\omega)$ are the sound fields generated by the horizontal and vertical dipole, respectively. By considering the vertical and horizontal dipole components of the total sound field independently, it is easier to establish the effects of a solid boundary described, in the following section.

2.4 Monopole and dipole source models in a half-space

In the far-field, volcanic infrasound can be considered to propagate in a half-space. In this range and at low frequencies, irregular topography can be ignored so that the solid boundary can be approximated as being flat. Even though the ground surface absorbs some acoustic energy, especially in the high frequency range, it is assumed to be a rigid boundary due to a high contrast in acoustic velocity. If the plane is perfectly rigid, then the boundary condition requires that the normal fluid velocity is zero at the surface. This boundary condition can most easily be met using the image method. An image, S', having the same phase and magnitude as the source, S, is placed a distance z_0 below the boundary, and the boundary is removed. In other words the rigid part is replaced by air (Fig. 2.1c). The resulting sound waves generated by both source and image radiate into unbounded space satisfying the boundary condition. Naturally, only the region above the boundary plane contains the medium and carries acoustic energy. Conversely, the region below the boundary has no physical reality. Mathematically, the wavefield reflecting from the rigid plane represents the superposition of two wavefields generated by both source and image. Hence, the Green's function for a half-space can be written in terms of two Green's functions in a free space (Morse and Ingard, 1986)

$$g_\omega(\mathbf{r}|\mathbf{r_0}) = G_\omega(\mathbf{r}|\mathbf{r_0}) + G_\omega(\mathbf{r}|\mathbf{r'_0}), \tag{2.14}$$

where $\mathbf{r_0} = (x_0, y_0, z_0)$, $\mathbf{r'_0} = (x_0, y_0, -z_0)$, and $G_\omega(\mathbf{r}|\mathbf{r'_0})$ is Green's function for the image in a free-space.

2.4.1 Monopole source

Monopole radiation in a half-space can be easily solved by replacing the Green's function, G_ω in Eq. (2.6) with g_ω

$$\begin{aligned}
\hat{p}(\omega) &= -ikc\hat{S}(\omega)g_\omega(\mathbf{r}|\mathbf{r_0}) \\
&= -ikc\hat{S}(\omega)\left[G_\omega(\mathbf{r}|\mathbf{r_0}) + G_\omega(\mathbf{r}|\mathbf{r_0'})\right] \\
&= -ikc\hat{S}(\omega)\left[\frac{1}{4\pi R}e^{ikR} + \frac{1}{4\pi R'}e^{ikR'}\right]. \qquad (2.15)
\end{aligned}$$

At distances R from the source, which are much larger than the source is from the origin (i.e., for $R \gg r_0$), the two waves combine to form what appears to be a single, non-simple source at the origin. When $r \gg r_0$ and $\mathbf{r_0} = (0, 0, z_0)$,

$$\begin{aligned}
R &= |\mathbf{r} - \mathbf{r_0}| \simeq r - z_0\cos\theta, \\
R' &\simeq r + z_0\cos\theta, \qquad (2.16)
\end{aligned}$$

then,

$$\begin{aligned}
\hat{p}(\omega) &\simeq -\frac{ikc\hat{S}(\omega)}{2\pi r}\cos(kz_0\cos\theta)e^{ikr} \\
&\simeq -\frac{ikc\hat{S}(\omega)}{2\pi r}e^{ikr} \quad (\text{if } kz_0 \ll 1). \qquad (2.17)
\end{aligned}$$

If $kz_0 \ll 1$, i.e. if the location of the source above the boundary is considerably less than a wavelength, the far field is very weakly dependent on θ, thus resembling the far field from a simple source with strength $2\hat{S}(\omega)$ at the origin. The effective strength is doubled because the reflected wave adds to the initial wave in this case; the source and image are close enough together to be considered a single source of

double strength. The transient solution (Lighthill, 1978) in the time domain becomes

$$p(\mathbf{r},t) = \frac{1}{2\pi r}\dot{S}(t-\frac{r}{c}). \tag{2.18}$$

2.4.2 Dipole source

As in the monopole case, dipole radiation in a half-space can be obtained from the Green's function shown in Eq (14). If the source at z_0 is a dipole of strength $\hat{\mathbf{D}}(\omega)$ inclined at angle θ with respect to the vertical axis, then the mirror image will have the same x and y components as the source, but a D_z opposite in sign from that of the source. Therefore the total sound field is

$$\begin{aligned}\hat{p}(\omega) &= -ikc\hat{\mathbf{D}}(\omega)\cdot\nabla_0 g_\omega(\mathbf{r}|\mathbf{r_0}) \\ &= -ikc\hat{\mathbf{D}}(\omega)\cdot\nabla_0\left[G_\omega(\mathbf{r}|\mathbf{r_0}) + G_\omega(\mathbf{r}|\mathbf{r_0'})\right]\end{aligned} \tag{2.19}$$

Using the same approximations for R and R', and $kr \gg 1$ the far field solution can be obtained as (Morse and Ingard, 1986)

$$\begin{aligned}\hat{p}(\omega) &\simeq -\frac{k^2c}{2\pi r}\left[\left(\frac{x}{r}\hat{D}_x + \frac{y}{r}\hat{D}_y\right)\cos(kz_0\cos\theta) - i\frac{z}{r}\hat{D}_z\sin(kz_0\cos\theta)\right]e^{ikr} \\ &= -\frac{k^2c}{2\pi r}\left[\left(\frac{x}{r}\hat{D}_x + \frac{y}{r}\hat{D}_y\right) - i\frac{z}{r}\hat{D}_z kz_0\cos\theta\right]e^{ikr}\end{aligned} \tag{2.20}$$

It is convenient to split the sound fields into two parts corresponding to the horizontal ($\hat{p}_{_H}$) and vertical dipole ($\hat{p}_{_V}$) sources

$$\hat{p}_{_H}(\omega) = -\frac{k^2c}{2\pi r}\left(\frac{x}{r}\hat{D}_x + \frac{y}{r}\hat{D}_y\right)e^{ikr} \tag{2.21}$$

$$= -\frac{k^2c}{4\pi r}\hat{D}_H\cos\phi e^{ikR} \tag{2.22}$$

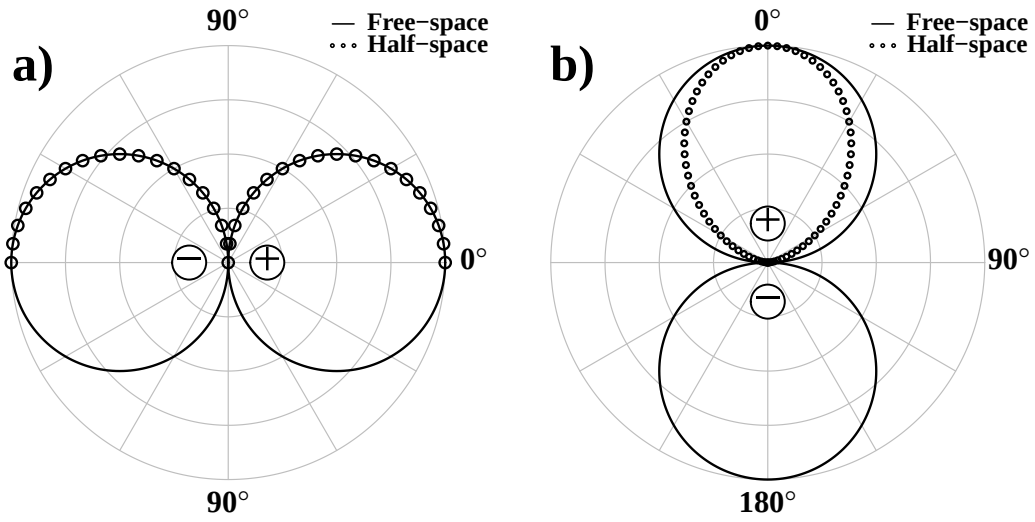

Figure 2.2: Theoretical directivity patterns for far-field sound pressure radiation from (a) horizontal dipole (Eq. 2.12 and 2.21) and (b) vertical dipole (Eq. 2.13 and 2.23). Pressures are normalized to their own maximum amplitudes.

$$\hat{p}_V(\omega) = \frac{ik^3c}{2\pi r}\left(\frac{z}{r}\hat{Q}_{zz}\cos\theta\right)e^{ikr} \tag{2.23}$$

$$= \frac{ik^3c}{2\pi r}\hat{Q}_{zz}\cos^2\theta e^{ikr} \tag{2.24}$$

where $D_H = \sqrt{\hat{D}_x^2 + \hat{D}_y^2}$, ϕ is an azimuth for the horizontal dipole axis and $\hat{Q}_{zz} = \hat{D}_z k z_0$. Since the dipole and its image become superimposed at large distances and for long wavelengths, the effective strength of the horizontal dipole above the half-space is doubled. The directivity pattern still depends on $\cos\phi$ as does the sound field from the horizontal dipole in a free-space (Fig. 2.2a). The radiation pattern from the vertical dipole is, however, different from that of a free-space. The effective strength is not just twice that of the source in a free-space, but depends on the distance z_0 from the boundary. The radiation pattern for the vertical dipole shows the $\cos^2\theta$ directivity. The pressure disturbances have a maximum magnitude on the dipole axis and attenuate much faster than that of the vertical dipole in a free-space as the angle θ approaches to 90° (Fig. 2.2b). This radiation pattern is that of a longitudinal quadrupole in a free-space, as one would expect from Figure 2.1d (Pierce, 1989).

The transient solutions for the far field are obtained as follows:

$$\begin{aligned} p_{_H}(\mathbf{r},t) &= \int_{-\infty}^{\infty} \hat{p}_{_H}(\omega) e^{-i\omega t} d\omega \\ &= \frac{1}{2\pi r c}\left[\frac{x}{r}\ddot{D}_x(t-r/c) + \frac{y}{r}\ddot{D}_y(t-r/c)\right] \end{aligned} \tag{2.25}$$

$$\begin{aligned} p_{_V}(\mathbf{r},t) &= \int_{-\infty}^{\infty} \hat{p}_{_V}(\omega) e^{-i\omega t} d\omega \\ &= \frac{1}{2\pi r c^2}\left[\frac{z}{r}\frac{\partial^3 Q_{zz}(t-\frac{r}{c})}{\partial t^3}\cos\theta\right] \end{aligned} \tag{2.26}$$

These solutions can be used for the inversion of the source time function using the method described in Section 4.

2.5 Inversion for source parameters

The inversion method for acoustic source parameters was developed based on the half-space model. An acoustic source from a volcano might be simulated as a combination of a monopole, dipole, and quadrupole in the view of the point source approximation. In this paper only monopole and dipole sources are taken into account. Since the source dimension is small with respect to the wavelength, quadrupole sources are comparatively less efficient. By excluding quadrupole sources the inverse problem is simplified. Even though quadrupole sources are not included in our inversion scheme, volcanic infrasound with large-scale jet noise may be affected by quadrupole sources (Matoza et al., 2009). A combined monopole/dipole source radiating into a half-space can be expressed as follows:

$$p(\mathbf{x},t) = p_{_M} + p_{_H} + p_{_V} \tag{2.27}$$

where $p_{_M}$, $p_{_H}$, and $p_{_V}$ are the sound field excited by a monopole, horizontal dipole, and vertical dipole respectively. In many field experiments, acoustic sensors are placed only on the ground which can be considered as a horizontal plane. Because the acoustic pressure from the vertical dipole decreases steeply as its deviation from the dipole axis increases (Fig. 2.2b and Eq. 2.24), $p_{_V}$ produces only a small contribution to the total sound field near the ground surface. Inversely, low level noise with observations recorded near the ground can induce large errors in source estimates for the vertical dipole. By ignoring the vertical dipole, pressure disturbances near the surface are rewritten in terms of Eq. (2.18) and Eq. (2.25):

$$p(\mathbf{r},t) = \frac{1}{2\pi r}\left[\dot{S}(t-\frac{r}{c}) + \frac{x}{cr}\dot{F}_x(t-\frac{r}{c}) + \frac{y}{cr}\dot{F}_y(t-\frac{r}{c})\right] \tag{2.28}$$

The horizontal dipole was defined as $\mathbf{F} \equiv \dot{\mathbf{D}}$, which is force in units of $kg\cdot m/s^2$. A set of linear equations can be derived from approximation of a continuous relationship by a discrete representation. Let p_i be the infrasound record obtained from the ith station,

$$p_i^k \equiv p_i(t_0 + k\Delta t - \frac{r}{c}) \tag{2.29}$$

so that p_i^k is the kth element of the time series. The model vector which contains unknown parameters is defined as follows:

$$\begin{aligned} \mathbf{m}^k &= \left[m_1^k, m_2^k, m_3^k\right] \\ &= \left[\dot{S}(t_0+k\Delta t), \dot{F}_x(t_0+k\Delta t), \dot{F}_y(t_0+k\Delta t)\right] \end{aligned} \tag{2.30}$$

From Eq. (2.28), the relationship between the observed data and the model vector is obtained,

$$p_i^k = \frac{1}{2\pi r_i}\left[m_1^k + \frac{x_i}{cr_i}m_2^k + \frac{y_i}{cr_i}m_3^k\right] \tag{2.31}$$

These linear equations allow a direct inversion of the infrasound records to obtain an estimate of the acoustic source parameters, as characterized by monopole strength and dipole vector. In presenting the details of the actual inverse method, it is convenient to write Eq. (2.31) in the common matrix form,

$$\mathbf{P}^k = \mathbf{G}\mathbf{m}^k \tag{2.32}$$

In this case, P^k is a vector of dimension n and is composed of sampled pressure disturbances observed from n stations. The matrix $\mathbf{G}$ is an $n \times 3$ matrix. In order to solve Eq. (2.32), the number of stations must be larger than three. Singular value decomposition of $\mathbf{G}$ is used and generalized inverse $\mathbf{G}^{-1}$ (Parker, 1994) is calculated. $\mathbf{G}$ can be decomposed as

$$\mathbf{G} = \mathbf{U}\mathbf{S}\mathbf{V}^T \tag{2.33}$$

where $\mathbf{U}$ consists of the eigenvectors associated with the nonzero eigenvalues of $\mathbf{G}\mathbf{G}^T$, $\mathbf{V}$ consists of similar eigenvectors for $\mathbf{G}^T\mathbf{G}$, and the diagonal members of $\mathbf{S}$ are the positive square roots of the nonzero eigenvalues of $\mathbf{G}^T\mathbf{G}$. The generalized inverse of $\mathbf{G}$ becomes

$$\mathbf{G}^{-1} = \mathbf{V}\mathbf{S}^{-1}\mathbf{U}^T \tag{2.34}$$

Equation (2.32) can be solved by taking the matrix inverse to obtain

$$\mathbf{m}^k = \mathbf{G}^{-1}\mathbf{P}^k \tag{2.35}$$

This equation provides a very general means of solving the inverse problem, but we need to evaluate the significance of the inverse.

2.6 Stability of inversion method

To obtain some measure of the fit resulting from the inversion procedure and to quantify the significance of the inversion, the variances of the model parameters are calculated. For statistically independent data the variance of the model becomes (Jackson, 1972)

$$var(m_j^k) = \sum_{i=1}^{n} (G_{ji}^{-1})^2 var(P_i^k) \tag{2.36}$$

As shown in Eq. (2.34), $(G_{kj}^{-1})^2$ is proportional to the reciprocal of the eigenvalues of $\mathbf{G^T G}$. Small eigenvalues will therefore lead to high uncertainty in m^k terms lowering the stability of the inversion. The stability can be characterized by the condition number of the problem (Stump and Johnson, 1977), defined as the ratio of the largest to smallest eigenvalues of $\mathbf{G^T G}$. Since the matrix $\mathbf{G}$ depends on receiver position and the sound speed ($\simeq 340 m/s$) in air according to Eq. (2.32), azimuthal distribution of stations is critical to the condition number.

A set of experiments examined the azimuthal dependency of the condition number. Source time functions for a monopole and dipole are taken to be gaussian functions with different wavelengths. From these sources, synthetic data were generated with 10% gaussian random noise for each station. Six different distributions of stations were tested and the condition number, model parameters, and their variances were calculated using Eq. (2.35) and Eq. (2.36). Mass flux $S(t)$ and the dipole vector $\mathbf{F}(t)$ were integrated from the model parameters (Eq. 2.30). The dipole vector was denoted by the magnitude $|\mathbf{F}|$ and the azimuth θ. The error associated with the numerical integration was ignored. Typically, for the trapezoid rule, the error terms are on the order of the square of time interval (Δt^2) of the data (Cheney and Kincaid, 2007). The exact magnitude of the error cannot be calculated without the original analytic function. Each configuration and results of each trial are given in Table 2.1.

While the inversion was successful, rather large condition numbers were yielded in

a) Trial 1

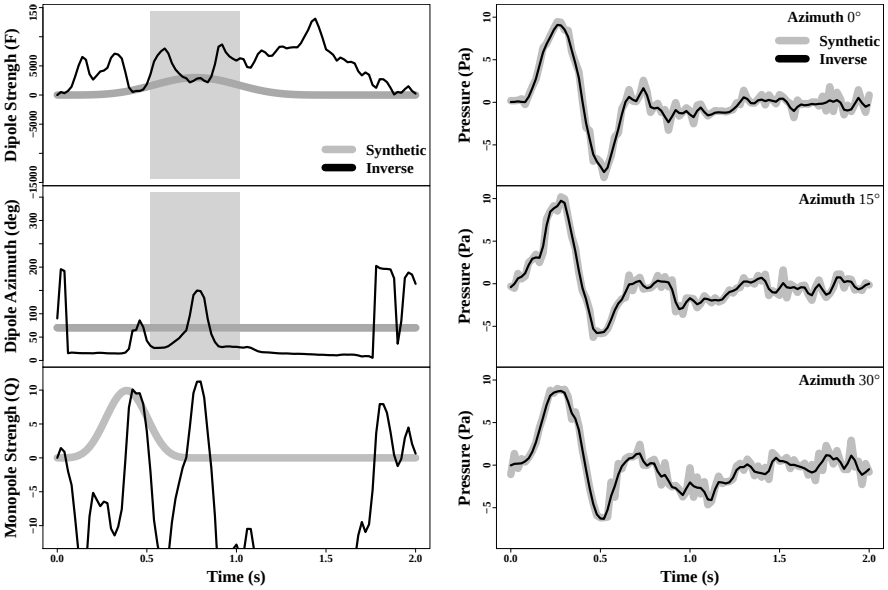

b) Trial 4

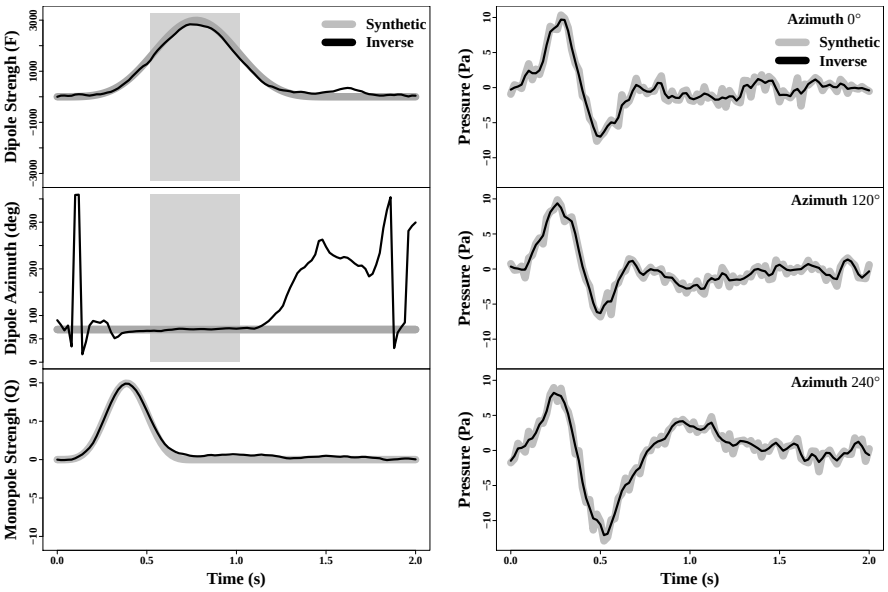

Figure 2.3: Comparison of Trial 1 (a) and 4 (b): Left columns show estimated source parameters. Fitted infrasound waveforms are given in the right columns. 10% gaussian random noise is added to the synthetic data. Both trials show good fits to the data. However, only source parameters from Trial 4 are reliable. Estimates of the dipole direction of Trial 4 show good agreements with those of the synthetic dipole in the shaded region where the dipole strength is above noise level.

Trials 1 and 2. Trials 3 and 4 also show successful inversion, although their condition numbers and standard deviations are significantly reduced. The result of fitting the data and estimated source parameters from Trials 1 and 4 are compared in Fig. 2.3. Even though both trials show good fits to the synthetic data, only the estimated source parameters from Trial 4 are reliable. Therefore, in order to achieve stable inversion, at least three stations covering 180° of azimuth are required. In Trials 5 and 6, the condition numbers are not reduced compared to Trial 4, though the standard deviations decrease continuously. The experiment suggests that doing the inversion at least 3 stations evenly distributed over 360° should produce the best result for the inversion.

Table 2.1: Estimates of the source parameters and their standard deviations for different station configurations.

Trial No.	Station Azimuth (°)	Condition No.	S	$\|F\|$	θ
Source			10 kg/s	3000 $kg \cdot m/s^2$	70°
1	0, 15, 30	4.4×10^8	0.4 (±29)	2817 (±8677)	150° (±112)
2	0, 45, 90	6.0×10^6	11 (±2.9)	2755 (±887)	73° (±19)
3	0, 90, 180	5.2×10^5	10 (±0.61)	2741 (±344)	67° (±5)
4	0, 120, 240	2.3×10^5	9.9 (±0.54)	2822 (±271)	71° (±5)
5	0, 90, 180, 270	2.3×10^5	10 (±0.46)	3080 (±234)	67° (±4)
6	0, 45, 90, 135, 180, 225, 270, 315	2.3×10^5	9.8 (±0.33)	3059 (±163)	70° (±2.9)

2.7 Infrasound radiation pattern and source characteristics

2.7.1 Field experiment

Tungurahua volcano is a large andesitic stratovolcano in the Cordillera Real of Ecuador. The active vent, 5023-m high, is located on the upper part of its northwestern flank. In May 2010, a new eruptive cycle began with a mid-size volcanic explosions associated with sustained ash column emissions, pyroclastic flows and seismic and infrasonic tremor.

Between 2006 – 2010 a network of five broadband seismo-acoustic stations was deployed by IGEPN (Instituto Geofísico – Escuela Politécnica Nacional, Ecuador), with support from Japan's JICA program to monitor Tungurahua for hazard mitigation and volcano research. Each station included an ACO Type-7144/4144 acoustic sensor. The nominal infrasound sensor response was 0.1 to 100 Hz, with microphone sensitivity 0.025 V/Pa and output voltage ±5 V. The amplifier-sensors were set to record 893.5 Pa at full scale with sensitivity -0.005593 V/Pa, and a 100 Hz lowpass filter was applied in the amplifier circuits. The microphones were designed specifically to record in harsh volcanic settings. Distances between the vent and stations range from 5.05 km at BPAT (Fig. 2.4) to 6.11 km at the furthest station BRUN.

Numerous infrasonic events were recorded during the period of May 28 – June 5. Tungurahua infrasound records are characterized by short impulsive onsets indicating explosive eruptions. The peak magnitudes of these events were very large, up to hundreds of Pa. The infrasound field recorded on the network exhibited clear directivity concerning radiation patterns: this strong directivity is not common in volcano infrasound. In most cases, the highest amplitudes were observed at station BBIL (Fig. 2.4). Although BPAT is the closest station from the active vent, recorded peak amplitudes were less than those at BBIL. The directivity of the radiation patterns

cannot be explained by a simple monopole source. Accordingly, a model with a dipole source may be required.

2.7.2 Inversion for source parameters

The multipole source model (monopole and dipole) was applied to the infrasound records from Tungurahua, and the waveforms were inverted for source parameters. Several assumptions were made: 1) We assumed that infrasound waves from Tungurahua propagate into a half-space. Because of the slope ($\approx 20°$) of Tungurahua, infrasound spreads out over wider region than that of a hemispherical half-space. In this case, inferred source strength from the half-space assumption is less than that of the "true" source. 2) the acoustic wave intrinsic attenuation was ignored. Within the lower atmosphere, the attenuation coefficient for frequencies ranging from 0.05 – 4 Hz is smaller than about 10^{-6}dB/m which corresponds to a 0.1dB loss over a 100-km path length (Sutherland and Bass, 2004; de Groot-Hedlin, 2008). Hence over the 5–10 km distance in our experiment, intrinsic attenuation is negligible. 3) Secondary propagation effects such as reflection, refraction, and diffraction were not considered. At short range and low elevation, the atmosphere is considered to be homogeneous. Irregular topography was also ignored. BULB and BRUN were potentially affected by reflection or refraction from local complex geometry. However, because there were no barrier in the line between the vent and the stations and only short impulsive events were chosen, the first single oscillation of signal is likely to be less affected by reflection and refraction. 4) Wind effects are also ignored. Wind usually affects the infrasound amplitude: a station in the upwind direction records larger amplitudes than one in the downwind direction. Theoretically if the wind speed is Mach number 1, then the ratio of upwind to downwind amplitude is about 1.5 in a homogeneous atmosphere (Ostashev et al., 2005). During deployments in May and June 2010, winds had a mean velocity of 6.3 $\pm$ 5.5 m/s to the WNW direction, estimated from

Table 2.2: Condition number and standard deviations of the source parameters for two events as shown in Fig. 2.5. S and $|F|$ denote monopole and dipole strengths, respectively. Percentages of the standard deviation with respect to the estimates are given in parentheses.

Event time	Condition No.	S (kg/s)	$\|F\|$ $(kg \cdot m/s^2)$	Azimuth (°)
2010-5-30, 16:43:44	3.0×10^5	$\pm 2.9 \times 10^4$ (4%)	$\pm 2.1 \times 10^7$ (9%)	$\pm 3.2°$
2010-5-30, 17:45:03	3.0×10^5	$\pm 2.7 \times 10^4$ (5%)	$\pm 2.0 \times 10^7$ (9%)	$\pm 3.5°$

wind models of the Ecuadorean Civil Aviation Agency. With such low speeds, wind effects on the sound amplitude are negligible. Since the peak amplitude ratio of BBIL to BPAT in most cases exceeds 2 or 3, the amplitude difference is likely caused by acoustic source characteristics rather than wind.

We selected 80 impulsive events during the period of the experiment, using only data with high signal to noise ratio (40± 7 dB). The 6-s length signals were inverted and source time functions for a monopole and dipole were simultaneously estimated using Eq. (2.32). Integrating the source time function, the monopole strength $S(t)$, horizontal dipole strength $F(t)$, and azimuth of the dipole axis were obtained (Fig. 2.5).

Because the amount of noise associated with the observations is unknown, it is impossible to calculate exact variances of inverted model parameters using Eq. (2.36). On the assumption of 10% noise with respect to maximum signal amplitude, theoretical variances of the model parameters can be estimated (Table 2.2). These variances do not represent "true" uncertainties underlying model estimates, but rather provide insight on how stable model parameters with respect to data variability. Since the signal-to-noise ratios for the selected events are high ($\geq$ 33 dB), potential error magnitudes associated with the events are not expected to exceed 10% of the signal amplitudes.

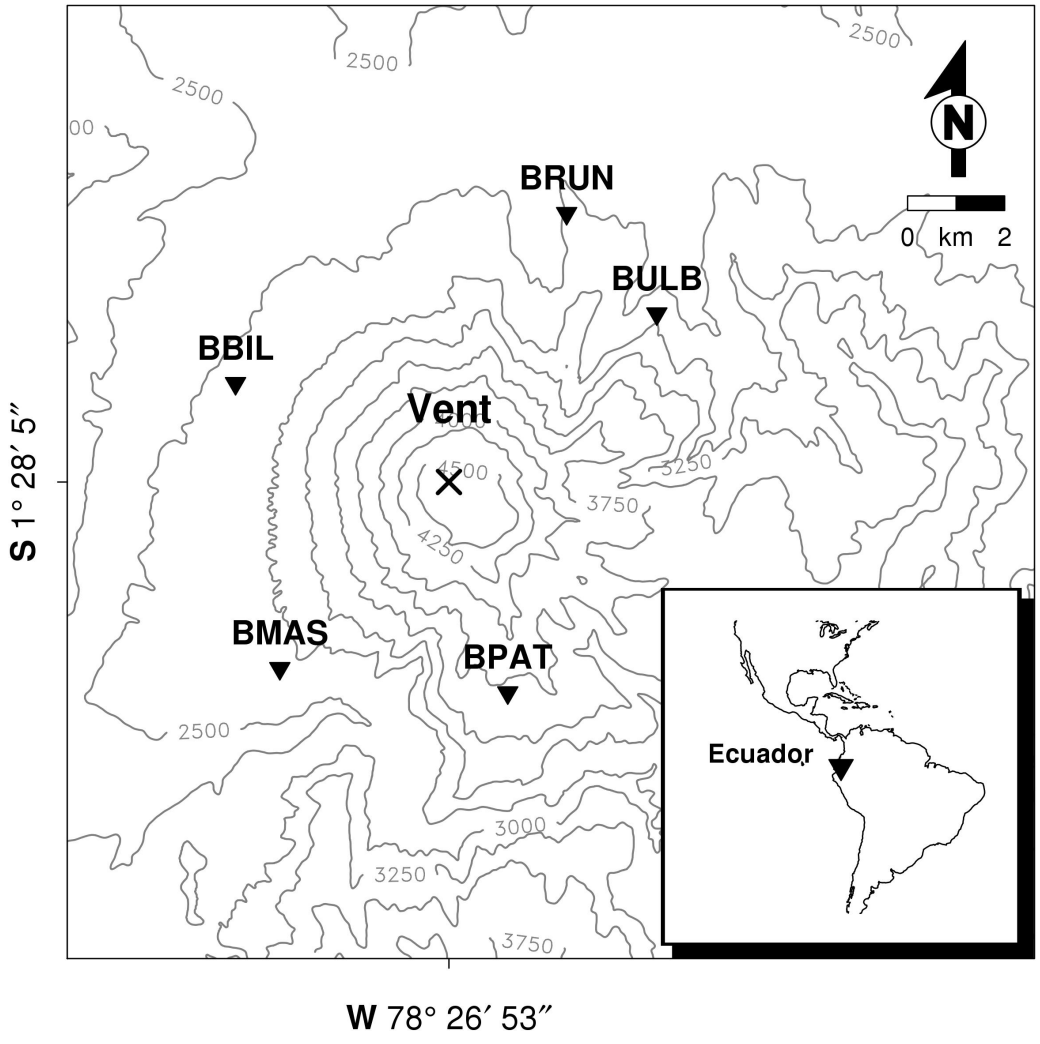

Figure 2.4: Map of Tungurahua volcano with the station geometry.

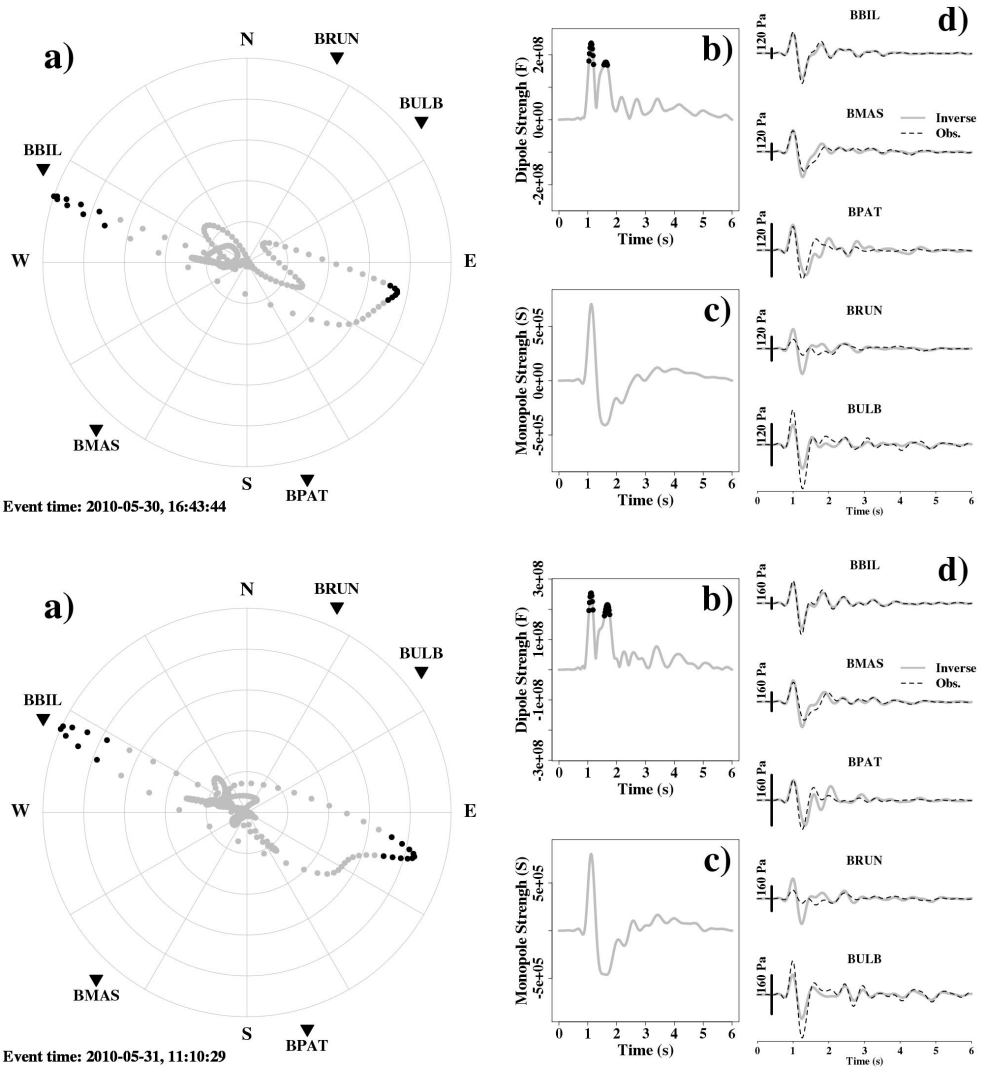

Figure 2.5: Data fitting and estimated source parameters for infrasound records from Tungurahua. The figure shows examples of two different events. a) Dipole direction over the source time function is plotted. The magnitude of the dipole is normalized to the maximum value of the source function. Both events show clear WNW directionality of infrasound radiation. Source time functions for b) a dipole and c) a monopole are shown. The dipole source function shows consistent directivity before and after the maximum amplitude of pressure (bold black line). d) The fit of observations and models is shown. The combination of the negative pressure of the dipole and the positive pressure of the monopole produced a small positive amplitude at BPAT. Most stations have acceptably good fits but BRUN exhibits a relatively large discrepancy. This might be attributed to the highly complex topography near the station.

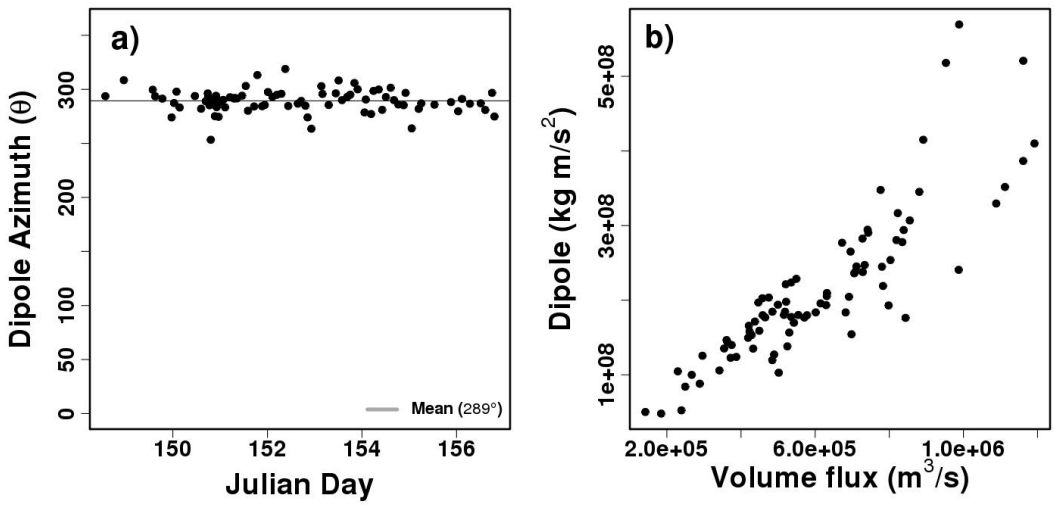

Figure 2.6: Estimated source parameters using events at Tungurahua volcano. a) Change of dipole azimuth during the field experiment. b) Volume flux estimated from monopole and dipole strengths.

2.7.3 Results

Two examples of the data fitting and estimated source parameters are provided in Fig. 2.5. In both cases the inversion results exhibit reasonably good fits to the data. The largest misfits were associated with stations BRUN and BULB. While the observed amplitudes from BRUN were consistently smaller than the fits, BULB showed larger amplitudes than expected from the inversion. These two stations were located in areas of complex terrain, with two wide and deep valleys nearby. Scattering and reflections may be caused by the complex topography and terrain fluctuation. However, our inversion procedure appears to be stable and the results are consistent (Fig. 2.5 and 2.6). We surmise that this is because we have used all the available stations for inversion and site effects are not appreciable, leading to predicted pressures that are close to observations.

The condition number for the network configuration is 3.0×10^5 (Table 2.2), larger than 2.3×10^5 for Trial 4, but much smaller than for Trial 3 (Table 2.1). Standard deviations for the monopole and horizontal dipole strengths are within 10% of their

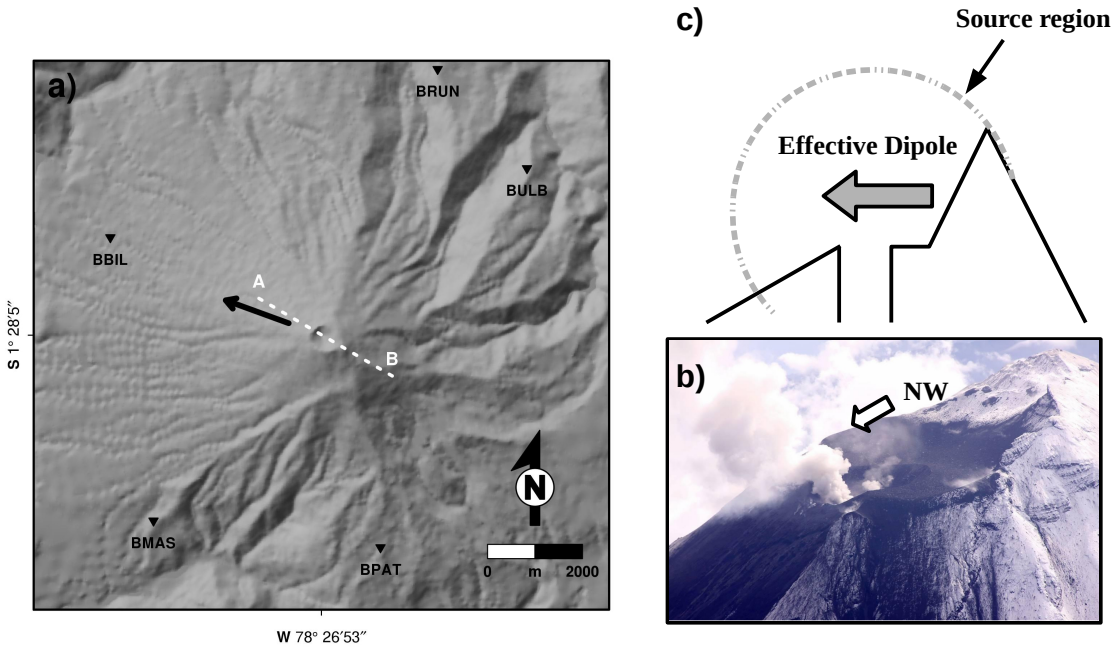

Figure 2.7: Crater geometry of Tungurahua volcano. a) The apparent direction of the vent-opening (line AB) closely matches the 289° mean azimuth (black arrow) of the dipole inverted from infrasound observations. b) Photo of the Tungurahua crater taken on 29 Nov. 2011. The crater is significantly asymmetric with longest diameter 500 m. The SE rim is about 300 meters higher than that of the NW. Photo courtesy of Patricio Ramón (IG). c) Schematic model of the effective acoustic dipole. The presence of the vent wall probably produces the effective dipole due to the interaction of fluid and sound with the solid boundary (see the text for details).

peak amplitudes. The low variances and associated condition numbers suggest that the inversion procedure is stable.

The computed dipole vectors (Fig. 2.6a) show a consistent direction with mean azimuth 289°. The dipole direction was compared with the crater geometry of Tungurahua. Tungurahua crater has a significant asymmetric shape (Fig. 2.7). The north-west wall of the crater is 300 m lower than the south-east wall, and the opening of the crater faces the north-west direction. The asymmetry of this feature was confirmed by visual observation during the field campaign. Taking into account the error of the DEM (produced by Instituto Geofísco Militar with 20 m resolution) and the geometry changes involved with explosive eruptions, the opening direction and the inferred dipole are considered to align significantly.

We also applied the simultaneous inversion method to "acoustic noise" that was not related to volcanic eruptions in order to check the site effects such as an instrument calibration and local noise. Noise data were chosen for different time periods over a week, and the dipole direction was estimated (see the online supplementary materials). Dipole directions from the noise were inconsistent with the 289° azimuth determined from the volcanic source and indicated which stations showed the highest noise level at that time. This suggests that the consistent dipole pattern observed from explosions was not caused by site effects.

Volume flux associated with volcanic explosions can be calculated from the estimated monopole strengths.

$$Q = \frac{1}{\rho_{air}} S(t), \tag{2.37}$$

where Q is volume flux, $\rho_{air} = 1\ kg \cdot m^3$ is the air density, and $S(t)$ is mass flux. The dipole and monopole strengths for events at Tungurahua are well correlated (Fig. 2.6b). Large explosions presumably generate strong dipole and monopole sources simultaneously. Estimated volume flux ranges between 10^4 and $10^6 m^3/s$. Tungurahua volcano has shown a wide range of eruption styles from Strombolian to Vulcanian.

During the experiment, it showed Vulcanian explosions with large ash columns and large amount of ballistics (Ruiz et al., 2006; Fee et al., 2010). We compared the volume flux with that of Augustine volcano, Alaska (Caplan-Auerbach et al., 2010). The volume flux of Vulcanian eruptions of Augustine in 2006 were estimated using infrasound observations to range between $2.6 - 6.2 \times 10^5 m^3/s$. Because the vent radius of Tungurahua ($\approx 100m$ on May 2011) is larger than that of Augustine ($\approx 30m$), it is reasonable that our estimated volume flux shows wider range, up to the order of $10^6 m^3/s$. We note that mass and volume outflux were estimated based on the assumption of the constant standard atmospheric density in the vicinity of the vent. If the vent is overpressurized or the volcanic jet significantly changes the composition of air near the vent, the assumption will likely introduce significant errors in the estimation. Even after taking the error of the density into consideration, however, the volume flux remains comparable to the previous results. This suggests that our multipole analysis is providing reasonable estimates of volume outflux during volcanic explosions.

The magnitude of the dipole vectors was compared with those calculated from observations at Mount Erebus, Antarctica (Johnson et al., 2008). The dipole vector from bubble bursts at the Mount Erebus lava lake was estimated using an acoustic dipole-solution in a free-space. The resultant dipole strength has a magnitude on the order of $10^7\ kg \cdot m/s^2$. The acoustic signals used for the inversion showed peak amplitudes of up to 200 Pa within a few hundred-meter distance from the source. Our results indicate dipole vectors ranging up to $10^8\ kg \cdot m/s^2$. Although the Tungurahua stations recorded 200 Pa peak at 5-km distance from the vent, the resulting dipole strengths are comparable to those of Mount Erubus. Because the dipole strength at Mount Erubus was calculated using a dipole-only model, the result may have been over-estimated by incorporating part of the monopole into the dipole radiation, as Johnson et al. (2008) noted. This may explain the similarity between dipole

strengths estimated for Tungurahua and Mount Erebus, although infrasound signals at Tungurahua volcano show much stronger amplitudes.

It should be noted that modeling presented here only accounts for the horizontal component of an arbitrary dipole in a half-space. The original dipole may include a vertical component, but it cannot be estimated with the present station configuration, as shown in Section 3. The real dipole may therefore be stronger than the estimated horizontal results reported here.

Since monopole, dipole, and quadrupole source models of volcanic infrasound have all been proposed (Woulff and McGetchin, 1976), it is still unclear which acoustic source type dominates during volcanic explosions. A monopole source model was used in studies of Strombolian explosions at Erebus and Karymsky (Lees et al., 2004; Johnson et al., 2004, 2008), a large rockfall at Mount St. Helens (Moran et al., 2008), and bubble oscillations at the lava surface at Shishaldin (Vergniolle and Caplan-Auerbach, 2004), Stromboli (Vergniolle and Brandeis, 1994) , and Erta Ale (Bouche et al., 2010). Only a few studies have addressed a dipole source model for volcanic explosions (Woulff and McGetchin, 1976; Vergniolle and Caplan-Auerbach, 2006; Johnson et al., 2008; Caplan-Auerbach et al., 2010). The acoustic network geometry may be one reason for the lack of dipole modeling; full three dimensional radiation patterns for a dipole solution are difficult to record on stations placed on the ground surface.

2.8 Discussion

In general the source of volcanic infrasound is associated with atmospheric vibration in the vicinity of the volcano vent. The acoustic source region is defined here by an artificial boundary that includes the vent (Fig. 2.7c). By incorporating the vent geometry in the source region, which is still compact compared to the source-receiver

distance, equations developed in Sec. 2 and 3 can be adapted for source inversion with no modification. Once we consider the source as compact, there is an equivalence between the multipole solutions and physical pressure fluctuations in the source region, similar to the force equivalence of a fault in seismology. In this section, we discuss several possible source mechanisms inside the source region, which are attributed to the inverted acoustic multipoles.

2.8.1 Direct Sources

Volcanic explosions and jets (or material flow) are direct sources of infrasound. Rapid expansion of the compressed gas caused by explosions can be modeled as an acoustic monopole, and represent the dominant source of the observed monopole. Moving objects that subsequently exert forces on the fluid, however, contribute as a dipole source. If the axis of the vent opening is inclined relative to the vertical axis, and materials are ejected in this direction, the resultant effect will be equivalent to a horizontal dipole component. Based on visual observation, the vent opening direction at Tungurahua volcano was not significantly tilted from the vertical. In this case, the vertical flow should be modeled as a vertical dipole, and the observed, strong, horizontal dipole is not accounted for.

2.8.2 Diffraction and Reflection

The interaction of sound with solid boundaries inside the source region may account for some of the observed radiation patterns. Theoretical calculations of sound reflection and diffraction using finite difference time domain (FDTD) method (Kim and Lees, 2011) can be compared to multipole approximations. The southeast vent wall at Tungurahua was represented by a semicircular, 200 m radial half disc, 200 m thick (Fig. 2.8a). Using the mirror image of the disc, sound radiation patterns were computed in the presence of the half-space. Because of azimuthal symmetry of the

computational domain, the three dimensional wavefield can be computed efficiently in the cylindrical coordinate (Kim and Lees, 2011). A homogeneous medium (air velocity = 340 m/s) was assumed and a monopole source of the gaussian function (1 Hz corner frequency) was used to excite the sound field. A dipole source was not used as the direct source because there is no evidence of significant horizontal fluid flow discussed in Section 7.1., and vertical dipole does not contribute to the horizontal asymmetric radiation. The frequency was estimated from observed infrasound which showed peak frequencies near 1 Hz, rapidly attenuating at higher frequencies. The source was placed on the disc axis by the wall illustrated in Fig. 2.8b. Sound pressures were obtained on the half-space boundary, 3 km distant from the source in all azimuthal directions, well enough away such that near-field effects can be ignored. Amplitudes, relative to the maximum amplitude in the propagating sound field, were then assumed to be measures of the effects of reflection and diffraction.

The modeled pressure distribution, compared with the multipole radiation pattern determined by observations, is shown in Fig. 2.9. The peak-amplitude ratios of each station relative to BBIL station are presented showing a considerable variance. The large variance is probably attributed to either complex source mechanisms which cannot be explained by the combination of the monopole and the dipole or to local noise at the stations. Because the amplitudes are ratios of each station to BBIL, local noise at BBIL has a compounding effect on variance in this plot. Even though the observed amplitudes show such a large variance, the inversion method appears to point to the best-fit solutions including a monopole and dipole.

While the monopole produces an omni-directional radiation, the dipole contributes to the varying amplitude dependent on the azimuthal direction. The dipole produces a positive amplitude of the first arrival in BBIL direction, which constructively interferes with the monopole amplitude. At the same time, a negative pressure of the first arrival is built up by the dipole in the opposite direction near station BPAT.

This destructive interference with the positive monopole produces a small, positive amplitude at BPAT. Because the observed dipole is alternating (Fig. 2.5a), the dipole direction is reversed after the first arrival, giving a large negative amplitude at BBIL and small negative amplitude at BPAT (Fig. 2.5d) due to interference with the negative monopole (Fig. 2.5c). Even though the strength of the dipole is larger than the monopole by an order of $\sim 10^2$ (Fig. 2.6), the combined radiation pattern shows positive amplitudes of the first arrival at all five stations. Because a dipole is represented by two alternating, closely spaced, monopole sources, the radiated energy cancels, and is a much less efficient source than a monopole source (Lighthill, 1952).

The diffraction (and reflection) shows the characteristic directional pattern presented in Fig. 2.9. The smallest radiation amplitude does not occur immediately behind the wall, but rather appears slightly off that direction. This is because edge-waves diffracted at the edge of the disc are superposed constructively at the axis of the disc, and destructive interference occurs slightly off the axis. In comparison with the multipoles, the directivity of the diffraction is remarkably aligned with it. The diffraction pattern explains well the large amplitude at BBIL and the small amplitude at BBAT. However, it is evident that the degree of directivity of the multipole is larger than expected from the theoretical diffraction pattern. The observed ratio of BPAT to BBIL (median value $\simeq 0.15$) is smaller than the value of 0.4 expected from the diffraction alone, suggesting that the amplitude of BBIL is much larger. This discrepancy is too large to be explained by modeling errors associated with the simplified model. Of course, assumptions of a semicircular back-wall and inaccurate wall dimensions may give rise to errors in the obtained diffraction pattern. At low frequency (1 Hz peak frequency, wavelength = 340 m), however, variations in wall dimensions of up to several tens of meters will not affect the diffraction radiation patterns significantly. This suggests that the diffraction effects partially influenced observed directivity, although other factors must have a significant impact on the

additional variation of directivity.

2.8.3 Aerodynamic Flow

In the previous section, we considered interaction of acoustic waves, generated by fluid flow, with solid boundaries in terms of diffraction and reflection. If solid boundaries are present in the source region and vent dimensions cannot be ignored compared to wavelengths, interaction between the material fluid flow (not sound) and solid boundaries may play an important role in sound production (Lighthill, 1952). Effects of solid-fluid interactions can be shown to be equivalent to a distribution of dipoles representing the force with which the solid boundary acts upon the fluid (Curle, 1955; Leehey and Hanson, 1970). In volcanology, sound emitted by a steady gas jet carrying solid fragments has been previously accounted for by a dipole (Woulff and McGetchin, 1976; Vergniolle and Caplan-Auerbach, 2006). The earlier studies considered the solid-fluid interaction (gas jet and solid particles or gas jet and solid wall) to be the sources of the dipole. In our study, explosion sources are dominant in the observed signals as opposed to steady gas jetting observed earlier. Rapid expansion of gas probably interacts with the vent wall, exerting significant forces on the flow. This exerting force should behave as an acoustic dipole. Because the vent wall of Tungurahua is asymmetric, the induced dipole is aligned with the normal to the wall surface.

We have proposed three possible source mechanisms based on observations and numerical modeling. The multipole source, inverted from the observations, showed a strong dipole component, significantly stronger than that expected from the diffraction modeling. The source physics that explains the multipole radiation is very likely to be non-unique because the multipole analysis calculates approximated acoustic sources that are equivalent to the source physics occurring during volcanic explosions. Different source mechanisms can obviously generate the same radiation pattern. It is

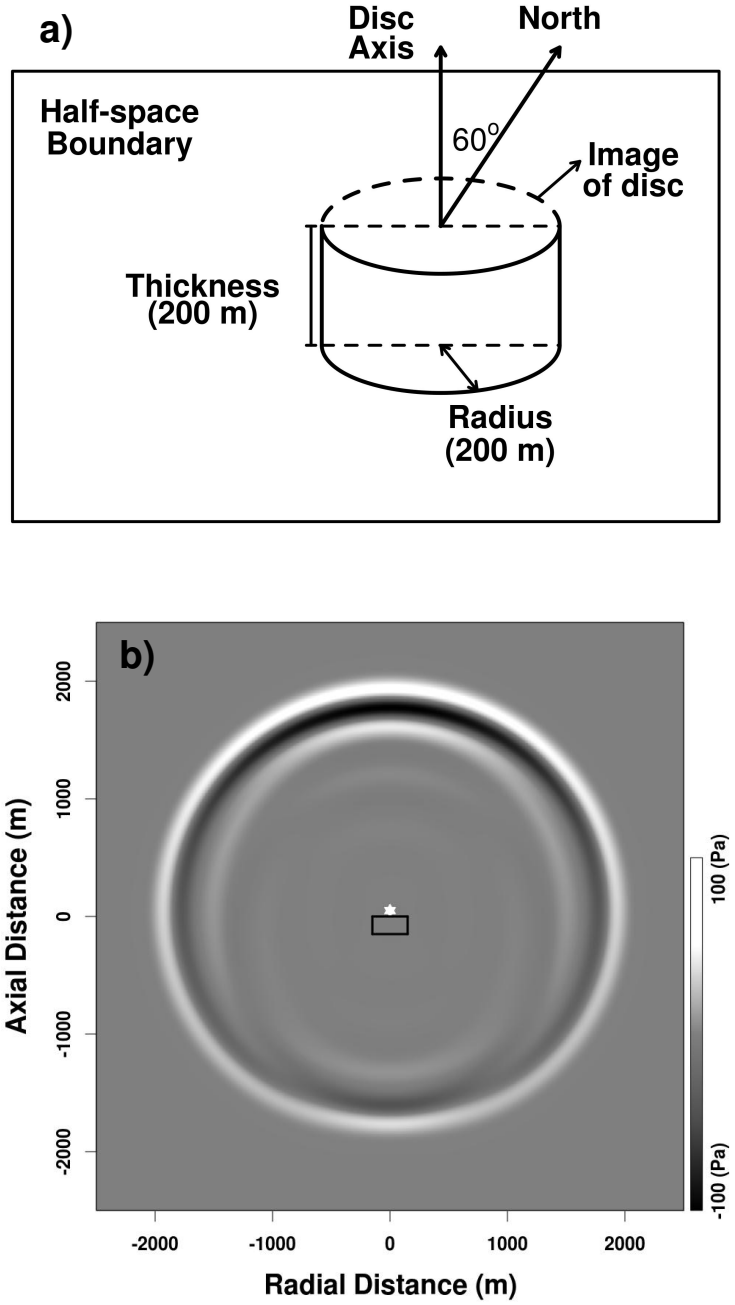

Figure 2.8: a) Configuration for FDTD modeling. The rigid half-space was achieved by the image of the disc. b) Snapshot of sound radiation near the disc. The source was excited by a monopole on the center of the disc.

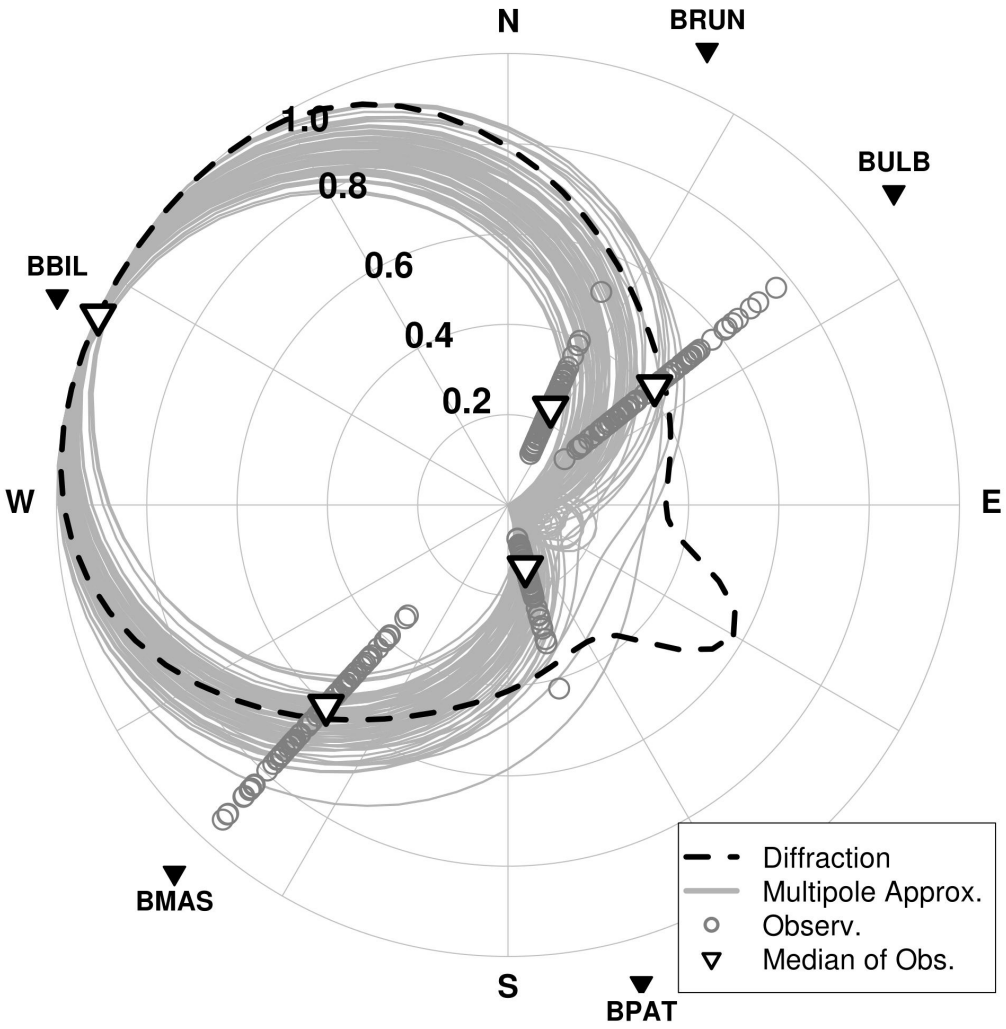

Figure 2.9: Comparison between the diffraction pattern (dot line) and the multipole approximation (grey solid lines). All curves are normalized to maximum values. Observed pressures (circles) at stations are over-plotted, and median values are indicated by invert triangles. The directivity of the diffraction is well aligned with the multipole approximation, but the small amplitude of BPAT cannot be explained solely by the diffraction (see the text for details).

important to note that sound diffraction by and fluid interaction with the asymmetric vent wall are both possible origins of the observed strong dipole radiation pattern. In both cases, the vent wall plays a critical role in developing the observed dipole radiation. The amount of mass outflux accompanied by explosions can be approximated by the strength of monopole component, if we assume the dipole component is produced by the effects of the wall. Even if the interaction with the vent wall does not exactly match the predicted dipole, this approximation should be useful in practice, especially when the number of stations in volcanic infrasound networks is limited.

2.9 Conclusion

We have derived approximate solutions for acoustic radiation in a rigid half-space and shown how to calculate the infrasound-acoustic response of waves emanating from volcanic explosions. The result indicates that a vertical dipole does not contribute to pressure disturbances near the half-space boundary (earth's surface) and inversion using this assumption should be treated with caution. A reliable inversion procedure was presented for estimating mass outflow and force generated during volcanic explosions. Monopole and dipole sources were simultaneously inverted for, and stable acoustic source parameters were extracted using at least three stations. The method was applied to observations at Tungurahua volcano in Ecuador, where mass outflux and dipole strength exhibited good agreement with previous estimates at other locations around the globe. We relate the acoustic amplitude directivity of explosions at Tungurahua to vent geometry. The approach taken was completely general and will be applicable to in other volcanic settings where extracting parameters of source dynamics are critical.

CHAPTER 3.

Source mechanism of Vulcanian eruption

3.1 Abstract

Source mechanisms of explosive volcanic eruptions are critical for understanding magmatic plumbing systems and magma transport. Because the open vent of a volcano is a corridor connecting the solid earth to the atmosphere, explosive eruptions efficiently excite both acoustic-infrasonic and seismic waves. Each of these mechanical waves carries characteristic information on several stages of the eruption process, and the coupling of these processes should shed considerable light into volcano dynamics. Tungurahua is a large andesitic stratovolcano where seismo-acoustic data has been recorded over several years. In 2010 May, a new eruptive cycle began with a mid-size Vulcanian explosion followed by swarms of explosive eruptions. The 5-station seismo-acoustic network recorded significant seismic and infrasonic signals from the explosions. The explosive eruptions of Tungurahua are characterized by: 1) an initial vent explosion, 2) an emergent, compressional first motion seismic arrival, 3) followed by quasi-harmonic coda and volcanic tremor. The first compressional waves are inverted for the seismic moment tensors and single forces. The results point to an ellipsoidal magma cavity 1.6 km below ad 400 m north of the summit crater. The onset times of the surface explosions are estimated from infrasonic arrival times, and

suggest that the surface explosions were triggered by the deep seismic events. The explosions at the deep magma cavity may open a pathway for gases to escape, and the upward gas flow triggers the surface explosions.

3.2 Introduction

Explosive eruptions of Vulcanian type are characterized by instantaneous ejection of volcanic bombs, ash, and gases associated with strong air shocks and seismic events. The seismic events accompanying explosive eruptions, called 'explosion earthquakes' hereafter, have been studied by many researchers. Kanamori et al. (1984) investigated Mount St. Helens eruption in 1980 and showed that the explosion earthquakes can be modeled by a combination of a single force and an implosive source. Tameguri et al. (2002) showed that an isotropic expansion occurred at a depth of 2 km before the explosive eruption at Mt. Sakurajima. Iguchi et al. (2008) also observed an triggering expansion preceding the surface explosion at Sakurajima, Suwanosejima, and Semeru volcanoes. The explosion earthquakes provide invaluable information about the mechanism of volcanic eruptions and the dynamic conditions in the conduit.

Full waveform inversion for seismic moment tensors has been widely used to study source mechanisms of volcanic eruptions. The inversion technique was applied to very-long-period (VLP) seismic signals (2 s – 100 s periods) associated with volcanic eruption, and successfully extracted seismic moment tensors and single forces at a number of volcanoes including Erebus (Aster et al., 2008), Stromboli (Chouet et al., 2003; Auger et al., 2006), Etna (Cannata et al., 2009), Kilauea (Ohminato et al., 1998; Chouet et al., 2010; Chouet and Dawson, 2011), Augustine (Dawson et al., 2011), and Tungurahua (Kumagai et al., 2011). Because low-frequency seismic waves are less affected by path distortion, VLP waveforms better preserve information about source mechanisms compared to high frequency waves. Long-period (LP) signals are

also frequently used for the moment tensor inversion. Kumagai et al. (2005) inverted LP events and showed that the source mechanisms of LP events are closely related to resonance of crack and transport of magmatic fluid. Tameguri et al. (2002) used low-frequency explosion earthquakes to obtain the seismic moment tensor at Sakurajima. Ohminato et al. (2006) found dominant single-force components from inversion of explosion earthquakes at Asama volcano.

Infrasound observations of active volcanoes have been very common in recent decades. Volcano infrasound is effective for tracking and quantifying eruptive phenomena because it is sensitive to shallow volcanic process near the vent while seismic waves reflect both shallow and deep magmatic activities. Volcano infrasound has been used with seismic observations in many volcano studies. Onset time of the vent explosions was inferred by infrasound observations and compared to seismic source mechanisms (Ishihara, 1985; Tameguri et al., 2002). Energy of infrasound was compared to that of seismic waves to investigate relative energy partitioning during explosions (Johnson and Aster, 2005). Volcano infrasound is a useful complement to seismic observation.

In this study, we analyze Vulcanian eruptions at Tungurahua volcano, Ecuador in 2010. Source mechanism of explosive eruptions are investigated by inverting explosion earthquakes for the seismic moment tensor and single forces (Ohminato et al., 1998). We use infrasonic observations to determine timing differences between explosion earthquakes and surface explosions. The results indicate volumetric moment tensors with a significant downward single force at a depth of 1.6 km. Finally, we provide an interpretation of the moment tensor and the single force and discuss the source mechanisms of the explosive eruptions at Tungurahua.

3.3 Tungurahua Volcano and Seismo-Acoustic Data

Tungurahua Volcano ($1.45°S, 78.43°W$) is one of the most active volcanoes in Ecuador. It is located on the Eastern Cordillera of the Ecuadorian Andes, and has 5023-m-high summit with steep flanks and extreme relief. In 2010 May, a new eruptive cycle began with a mid-size Vulcanian explosion associated with ejection of bombs, sustained ash column emissions, and pyroclastic flows. After five hours of quiescence, the volcano commenced explosive swarm activity, including hundreds of events, up to June 18, when the volcano returned to quiescence.

Between 2006-2008 a network of five broadband seismo-acoustic stations (Fig. 3.1) was deployed by IG-EPN (Instituto Geofísico – Escuela Politécnica Nacional, Ecuador), with support from Japan's JICA program to monitor Tungurahua for hazard mitigation and volcano research. Each station included a broadband seismometer (Guralp CMG-40T) with flat response to velocity from 30 seconds to 50 Hz and an ACO Type-7144/4144 acoustic sensor. The nominal infrasound sensor response was 0.1 to 100 Hz, with microphone sensitivity 0.025 V/Pa and output voltage ±5 V. The sensors were set to record 893.5 Pa at full scale with sensitivity -0.005593 V/Pa, and a 100 Hz low-pass filter was applied in the amplifier circuits. The microphones were designed specifically to record in harsh volcanic settings. Distances between the vent and stations range from 4.7 km at BPAT to 6.5 km at the furthest station BRUN.

A massive swarm of seismo-acoustic events was recorded during the period of May 28 – June 5. An example of seismic records associated with the explosion at the summit crater is shown in Fig. 3.2. The event is characterized by 1) an initial vent explosion, 2) an emergent, compressional first motion seismic arrival near 20 s, and 3) following quasi-harmonic coda and volcanic tremor after 30 s (or long-period waves) (Fig. 3.2). Initial explosions at the crater usually exhibited high excess pressure ($\sim$ 300 Pa peak-to-peak amplitude) in the infrasonic band as well as in the audio band.

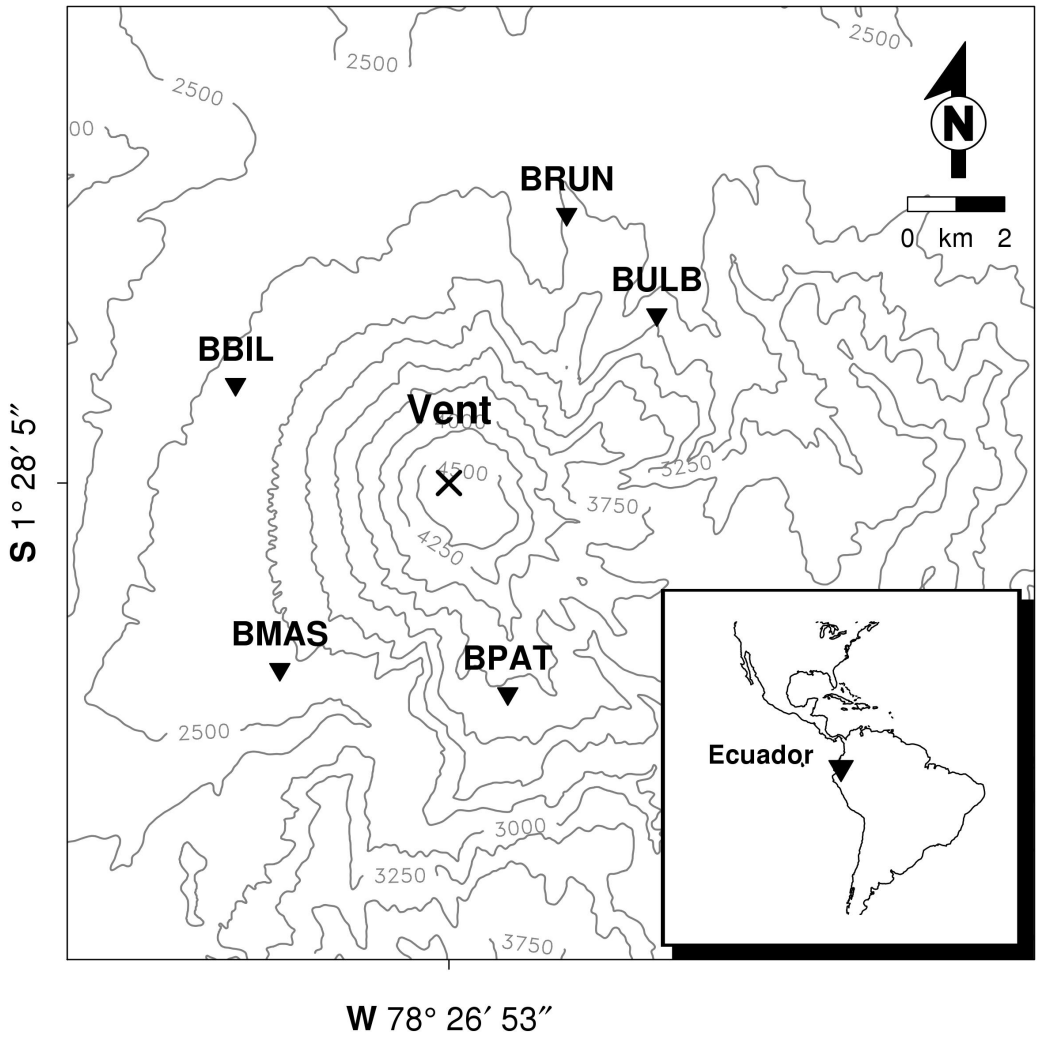

Figure 3.1: Map of Tungurahua volcano with the station geometry. Distance between the summit crater and stations range from 4.7 km at BPAT to 6.5 km at the farthest station BRUN.

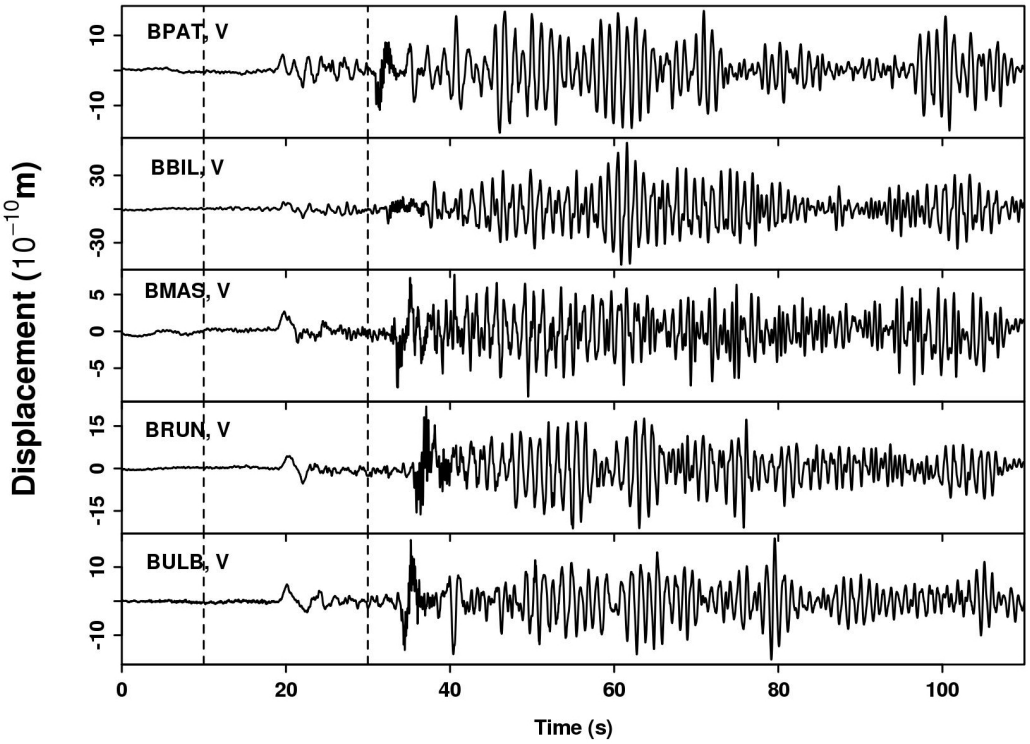

Figure 3.2: An example of seismic records associated with a crater explosion. Vertical components of displacement for Event 1 listed in Table 3.2 are shown over the five broadband stations. The signals are characterized by an compressional P-wave first motion emerging near 20 s and following quasi-harmonic coda and volcanic tremor.

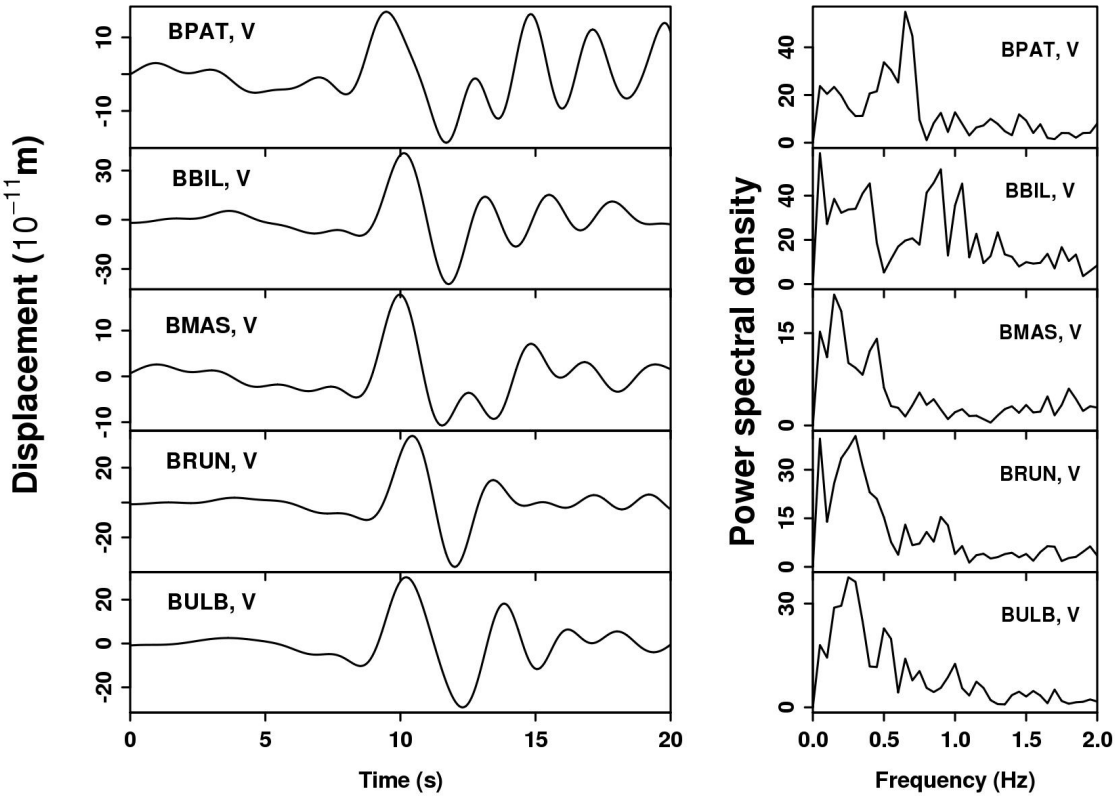

Figure 3.3: Band-pass filtered signals (10 s – 2 s) and power spectra of the first compressional motion between two vertical dot lines in Fig. 3.2. The signals show impulsive waveforms and have significant energy from 10 s to 2 s.

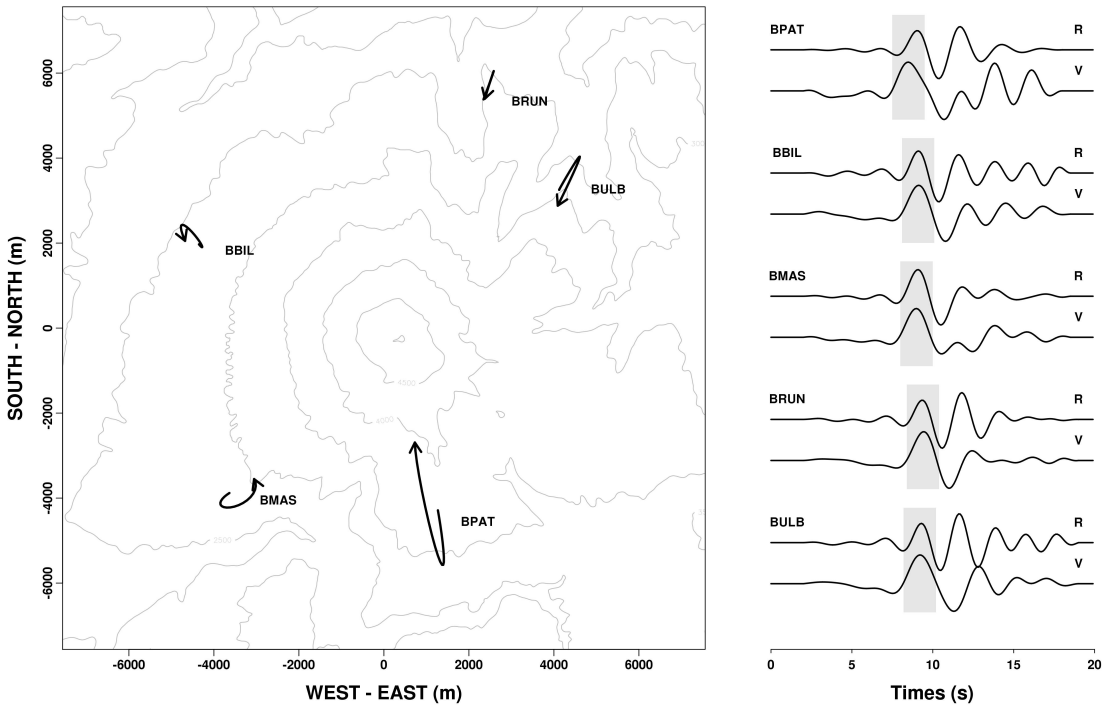

Figure 3.4: Particle motions observed on the network. The records shows the radial (R) and vertical (V) components of displacement in the right column. Signals are band-pass filtered in 10 s – 2 s band and normalized by component. P-wave first motions in the shaded region are compressional in all stations (up and away from the summit crater in the vertical and radial components, respectively) and is followed by a dilatational motion. Horizontal particle motions in the left column are rectilinear and point to the summit crater.

The first motion has significant energy in the 10 s - 2 s band (Fig. 3.3), and the band-pass filtered signals show impulsive waveforms. Fig. 3.4 shows particle motions of the first arrived phase. The horizontal particle motions are linearized in the direction of the summit crater, and the radial and vertical components are in phase. This result suggests that the first phase is composed of P-waves. P-wave first motions are compressional at all stations (up and away from the summit crater in the vertical and radial components, respectively) and is followed by dilatational motion. This suggests expansion and contraction with the explosion earthquake.

In this study, we select 10 explosion earthquakes (Table 3.2) which show signifi-

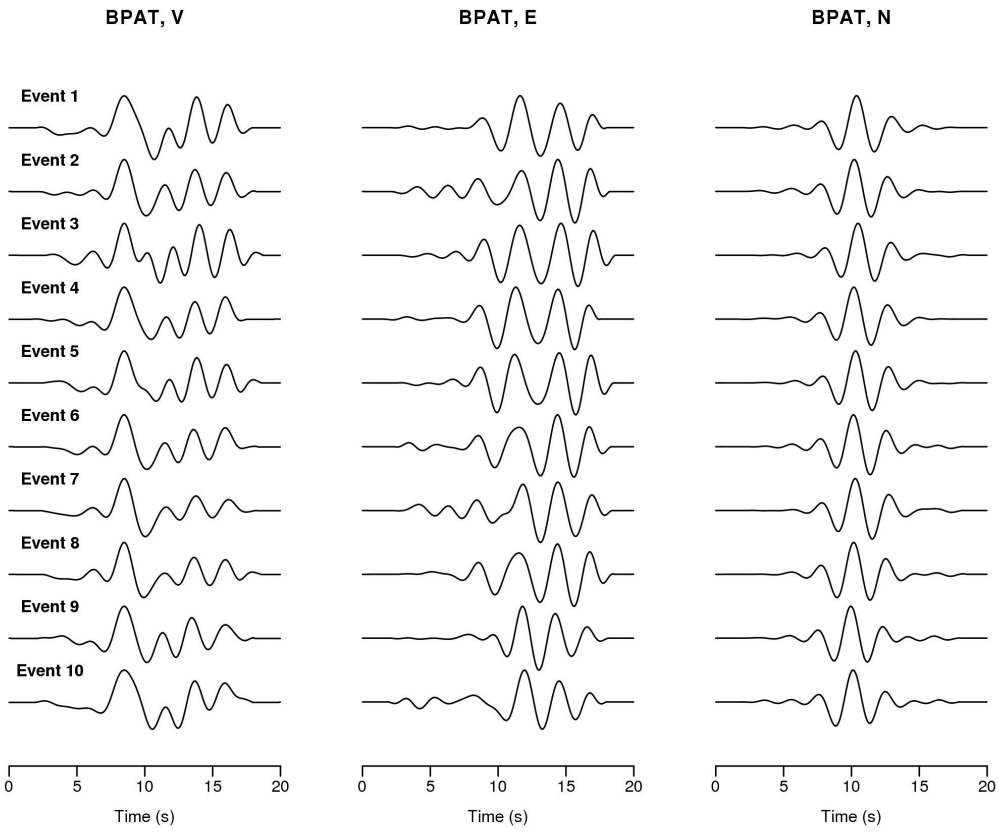

Figure 3.5: Seismic signals, band-pass filtered in 10 s - 2 s, recorded during explosive eruptions. Three components of displacement at BPAT station are displayed. The events are numbered in chronological order listed in Table 3.2.

cant P-wave first motions during the period of a massive swarm of explosive eruptions. Inversion technique (Ohminato et al., 1998) is used for source mechanism represented by six moments and three single forces. Displacement signals for the events at BPAT station are displayed in Fig. 3.5. All seismic signals show high correlations in waveforms. This similarity may reflect the repetitive activation of a nondestructive source process. We present source parameters obtained for the 10 events, but provide a full description only for Event 1 in Table 3.2. Because 10 events share common characteristics in the moment tensor solution, an analysis of a representative event describes the overall source mechanism.

3.4 Moment Tensor Inversion

The seismic displacement field can be expressed by a convolution of the Green's function with source terms (Chouet, 1996),

$$u_n(t) = F_p(t) * G_{np}(t) + M_{pq}(t) * G_{np,q}(t) \tag{3.1}$$
$$p, q = x, y, z,$$

where $u_n(t)$ is the n component of seismic displacement at a station at time t, $F_p(t)$ is the time history of the force applied in the p direction, $M_{pq}(t)$ is the time history of the pq component of the moment tensor, and $G_{np}(t)$ is the Green tensor which relates the n component of displacement at the receiver position with the p component of impulsive force at the source position. The notation $,q$ indicates spatial differentiation with respect to the q coordinate and the symbol $*$ denotes convolution. If we form the column vector $\mathbf{d}$ that contains the displacement components at all stations and column vector $\mathbf{m}$ containing the moment tensor and single force components, equation (3.1) can be rewritten in matrix form (Ohminato et al., 1998),

$$\mathbf{d} = \mathbf{G}\mathbf{m}. \tag{3.2}$$

Equation (3.2) is solved for $\mathbf{m}$ by minimizing the squared error, E,

$$E = \frac{1}{N_r} \sum_{n=1}^{Nr} \left[\frac{\sum_{1}^{3} \sum_{p=1}^{N_s} (u_n^0(p\Delta t) - u_n^s(p\Delta t))^2}{\sum_{1}^{3} \sum_{p=1}^{N_s} (u_n^0(p\Delta t))^2} \right] \tag{3.3}$$

where $u_n^0(p\Delta t)$ is the pth sample of the nth data trace, $u_n^s(p\Delta t)$ is the pth sample of the nth synthetic trace, N_s is the number of samples in each trace, and N_r is the number of three-component stations. In Equation (3.3), the squared error is normalized station

by station so that stations with weak-amplitude signals contribute equally to the squared error as stations with large amplitude.

A grid search is conducted to determine the best-fit source location. We search 440 grid points (Fig. 3.6) over the 8000 m $\times$ 8000 m $\times$ 8000 m gridded region in the east, north, and vertical directions, respectively. The grid spacing is finest near the vent region (up to 400 m spacing) and coarser further from the vent (up to 2000 m spacing). The least squares solutions to Equation (3.2) are computed with respect to all grid points, and the source location is determined by minimizing the squared error, E.

We consider three possible source mechanisms for the model parameters, $\mathbf{m}$: 1) six moments and three single-forces, 2) six moments, and 3) three single-forces. The optimum solution is chosen based on the squared error defined by Equation (3.3), relevance of the free parameters used in the model, and physical significance of the resulting source mechanism. Relevance of the free parameters in each model is assessed by calculating Akaike's information criterion (AIC) (Akaike, 1974),

$$\mathrm{AIC} = N_{obs} \ln E + 2N_{par}, \tag{3.4}$$

where $N_{obs} = 3 \times N_r N_s$ is the number of independent data, E is the squared error defined by Equation (3.3), $N_{par} = N_s \times$ (the number of source mechanisms) is the number of model parameters used to fit the data. The model is considered to be physically relevant if it minimizes both the squared error and AIC. Finally, physical plausibility of a moment tensor solution is considered. Consistent time history among all moment tensor components should be required to make a plausible interpretation of the solution.

The synthetic Green's functions are generated with a three-dimensional finite difference method (Ohminato and Chouet, 1997) taking into account the 3-D topography

of Tungurahua Volcano. For the edifice of the Tungurahua volcano, we assume a homogeneous velocity and density structure, a compressional wave velocity $V_p = 3.5$ km/s, shear wave velocity $V_s = 2$ km/s, and density $\rho = 2650$ kg/m^3 (Molina et al., 2005; Kumagai et al., 2011). The Green's functions are convolved with a cosine smoothing function to ensure inversion stability,

$$S(t) = \begin{cases} \frac{1}{2}\left[1 - \cos\left(\frac{2\pi t}{t_p}\right)\right], & 0 \leq t \geq t_p \\ 0, & t > t_p. \end{cases} \tag{3.5}$$

where $t_p = 2$ s.

Our computational domain is centered at the summit of Tungurahua and has lateral dimensions 40 $\times$ 40 km, and vertical divisions evenly spaced over 40 km, which is sufficiently large to avoid spurious edge reflection. The node spacing is 80 m, yielding a 3-D mesh with 500 $\times$ 500 $\times$ 500 nodes. While 25 nodes per wavelength are required for accurate modeling, 80 m spacing provides 50 nodes per wavelength (2000 m/s $\times$ 2 s = 4000 m) for signal frequencies considered in this study.

3.5 Result

3.5.1 Squared Error

We invert the 10 explosion earthquakes for source mechanisms assuming three different models: Model 1, six moments plus three single forces; Model 2, six moments only; Model 3, three single forces only. Minimum residual errors and AIC values for all the events are listed in Table 3.1. Residual errors and AICs of Model 3 are noticeably higher than those of other models over all the events. So, the third model option was eliminated from further consideration. Model 1 exhibits both the least residual errors and the lowest AICs for all the events. The synthetic waveforms corresponding

Table 3.1: Residual errors and corresponding Akaike's Information Criterion.

Event No.[a]	Model 1[b]		Model 2		Model 3	
	Error	AIC	Error	AIC	Error	AIC
1	0.11	-2932	0.28	-1368	0.45	-1182
2	0.11	-3026	0.25	-1707	0.49	-886
3	0.13	-2332	0.30	-1193	0.53	-691
4	0.12	-2732	0.27	-1501	0.49	-938
5	0.14	-2176	0.30	-1200	0.52	-718
6	0.14	-2274	0.27	-1490	0.52	-720
7	0.12	-2730	0.24	-1852	0.48	-950
8	0.16	-1872	0.30	-1174	0.53	-673
9	0.11	-2795	0.23	-1889	0.50	-835
10	0.10	-3257	0.24	-1782	0.45	-1148

[a] The event number denotes chronological order in Table 3.2.
[b] Model 1, 2, and 3 are composed of 6 moments plus 3 forces, 6 moments only, and 3 forces only, respectively.

to Model 1 fit the observed waveforms well (Fig. 3.7). The small AICs suggest that the reduction of residuals for Model 1 is not merely a numerical artifact caused by a large number of free parameters but has significance from a physical viewpoint.

3.5.2 Source Location and Source Time Function

The best-fit source locations and source time histories of the two models, Model 1 and 2, are investigated in this section in more detail. The minimum residual errors for Model 1 indicate the source 400 m north and 1.6 km below the summit crater (Fig. 3.6). Best-fit source hypocenters obtained for all the events lie at the same position. Even after accounting for the uncertainty of the grid search, consistent hypocenter locations suggests a repetitive activation of the same fixed source. Source time functions of six moments and three single forces for Event 1 are presented in Fig. 3.8. All six moments and single forces are geometrically consistent (Fig. 3.9). The solution can be interpreted as a crack-like mechanism with a downward vertical

force. In the next section, we discuss these source mechanisms in more detail. Source locations derived by assuming Model 2 lie 10 km below the crater. Since this is the deepest node layer of the grid search it is possible that the hypocenter solutions are actually deeper than our 3D model allows. This hypocenter is anomalously deep because our observation indicates that the seismic event occurred near the onset of the surface explosion. The seismic source probably lies at shallow region as does in Model 1 so that it directly affects the surface explosion. Source time histories of six moments are also unrealistic (Fig. 3.10). Spurious large amplitudes are required at the end of the time series to compensate for time series misfits caused by the early part of source time functions. All criteria including residual error, AIC, source location, and source time function indicate that Model 1 is the best model to describe observed waveforms.

3.5.3 Resolution of Single Forces

The capability of the inversion method to decouple single forces from moment tensor components is assessed by a synthetic test. The Green's functions produced by M_{zz} and F_z are similar, so that these components may be difficult to resolve when the station coverage is limited (Uhira and Takeo, 1994). Synthetic waveforms with 5% random noise are created by a point source at a depth of 1.6 km below the crater. The source mechanism is assumed to be a horizontal crack ($M_{xx} : M_{yy} : M_{zz} = 0.5 : 0.5 : 1$) with a simultaneous downward force (F_z/M_{zz} = -0.125 $\times 10^{-3}$). Note that a single force component is 1000 times more effective than a moment tensor component to excite the same amplitude of signal.

Overall fitting of solutions to the known source time functions are poor because of the added noise. The peak amplitudes of inversion solutions explain only 60% of those of the known source time functions in all components (Fig. 3.11). The ratios of M_{xx}, M_{yy}, and F_z to M_{zz} are, however, consistent with the original ratios. The downward

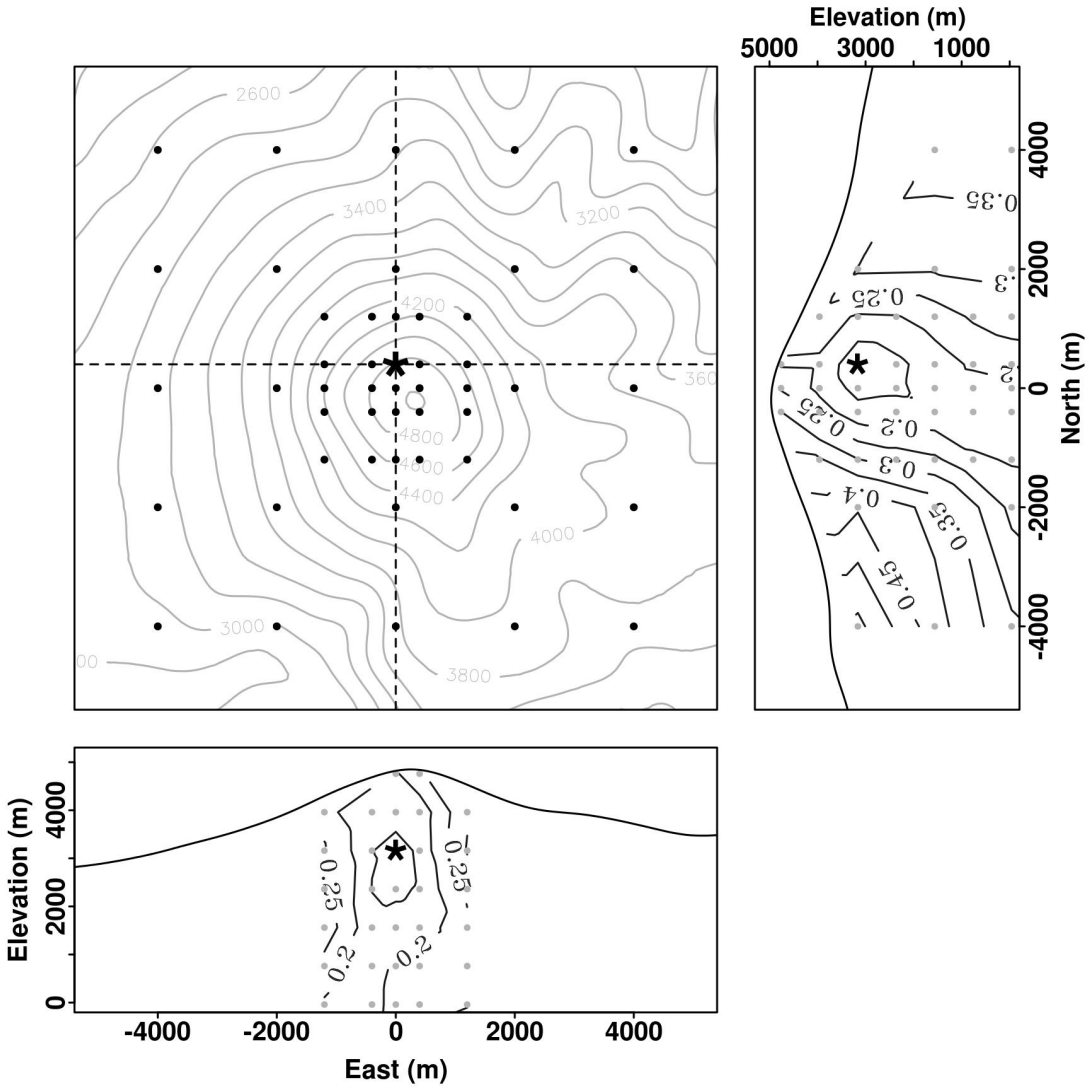

Figure 3.6: Best-fit source location (black star) of Event 1 obtained by assuming Model 1 lies 400 m north and 1.6 km below the summit crater. Residual error contours are shown in east-west and north-south cross sections through the point source. Dots indicate the nodes used in our grid search.

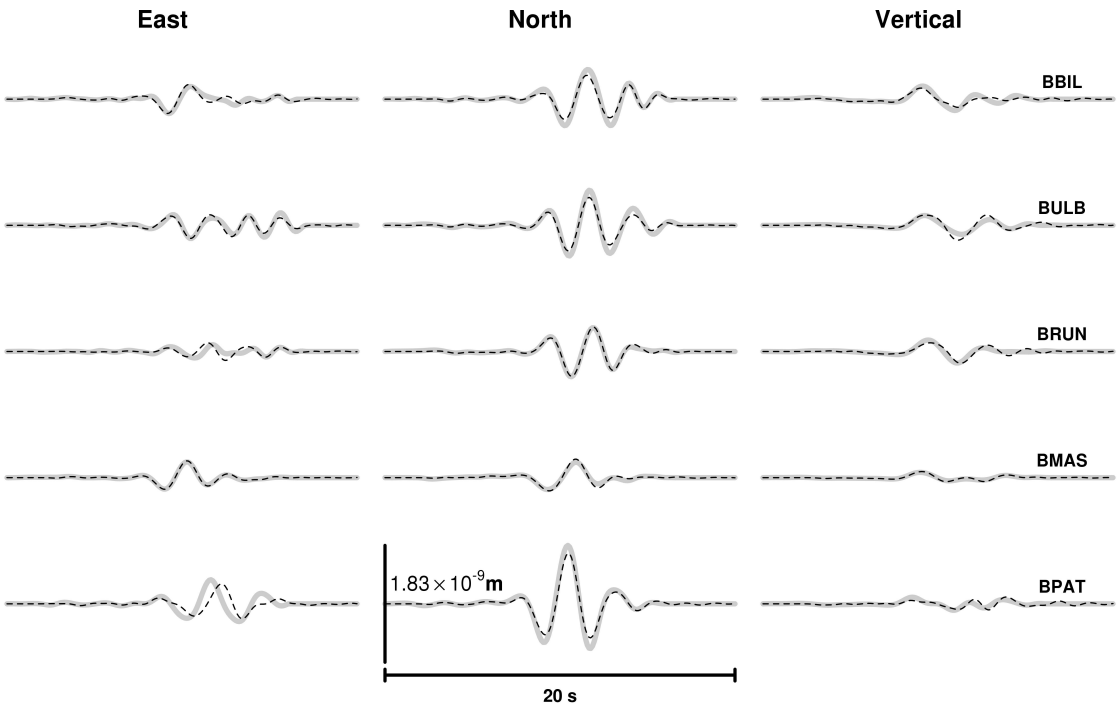

Figure 3.7: Waveform fit for Event 1 listed in Table 3.2. Thin dashed lines represent synthetic waveforms for Model 3. Thick solid lines are observed waveforms.

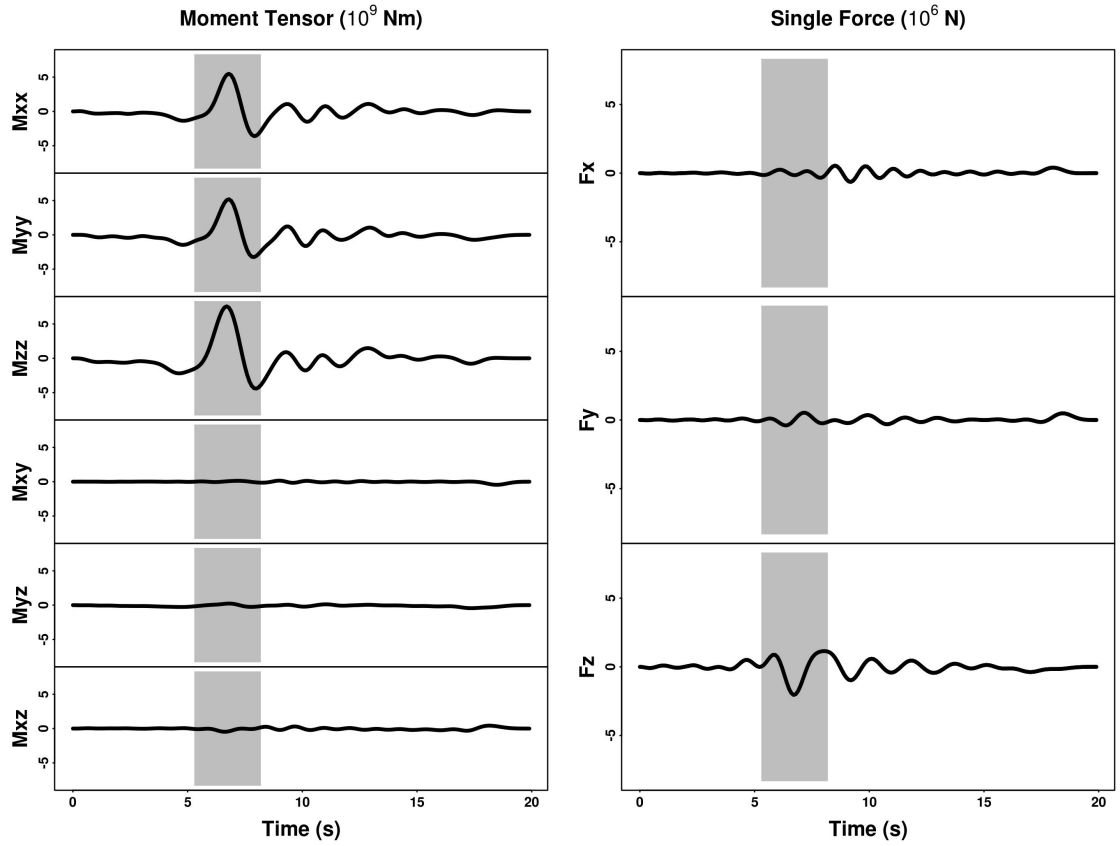

Figure 3.8: The source time functions of Event 1 for Model 1. Volumetric components (M_{xx}, M_{yy} and, M_{zz}) and a downward force (F_z) are dominant in the moment tensor and the single forces, respectively.

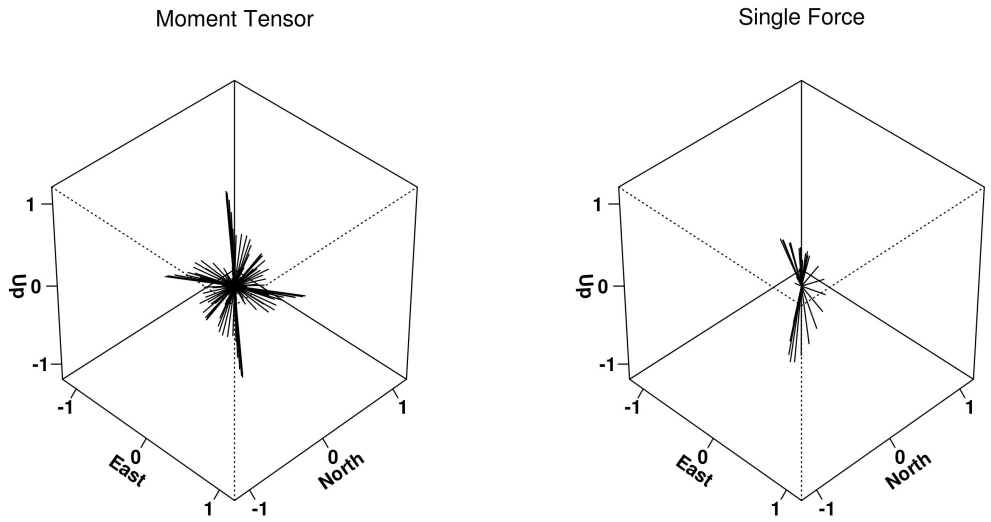

Figure 3.9: Three-dimensional representation of the eigenvectors (left) for the moment tensor and the resultant force (right) of the single forces. The shaded regions in Fig. 3.8 are plotted.

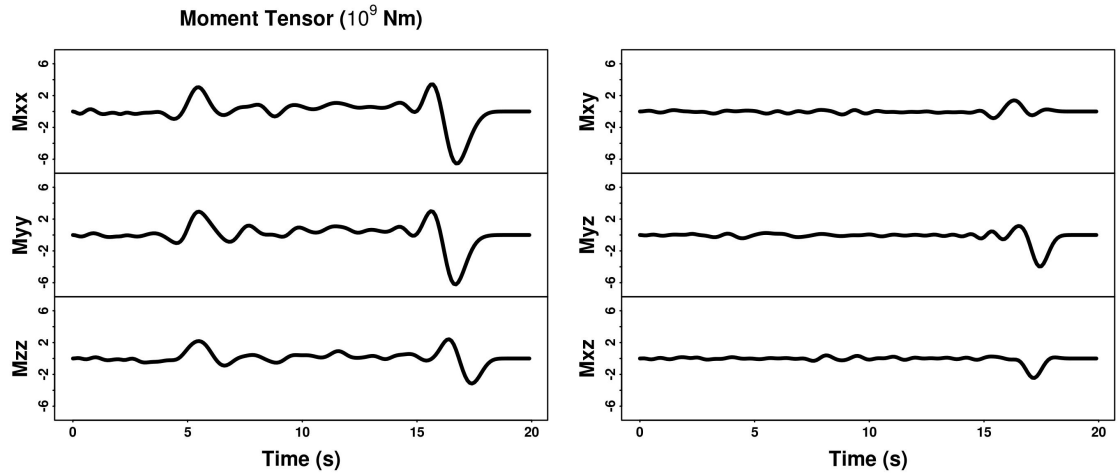

Figure 3.10: Source time functions of Event 1 obtained by assuming Model 2. The emergence of the large amplitude in the later part of the solutions suggests that this model is not reasonable.

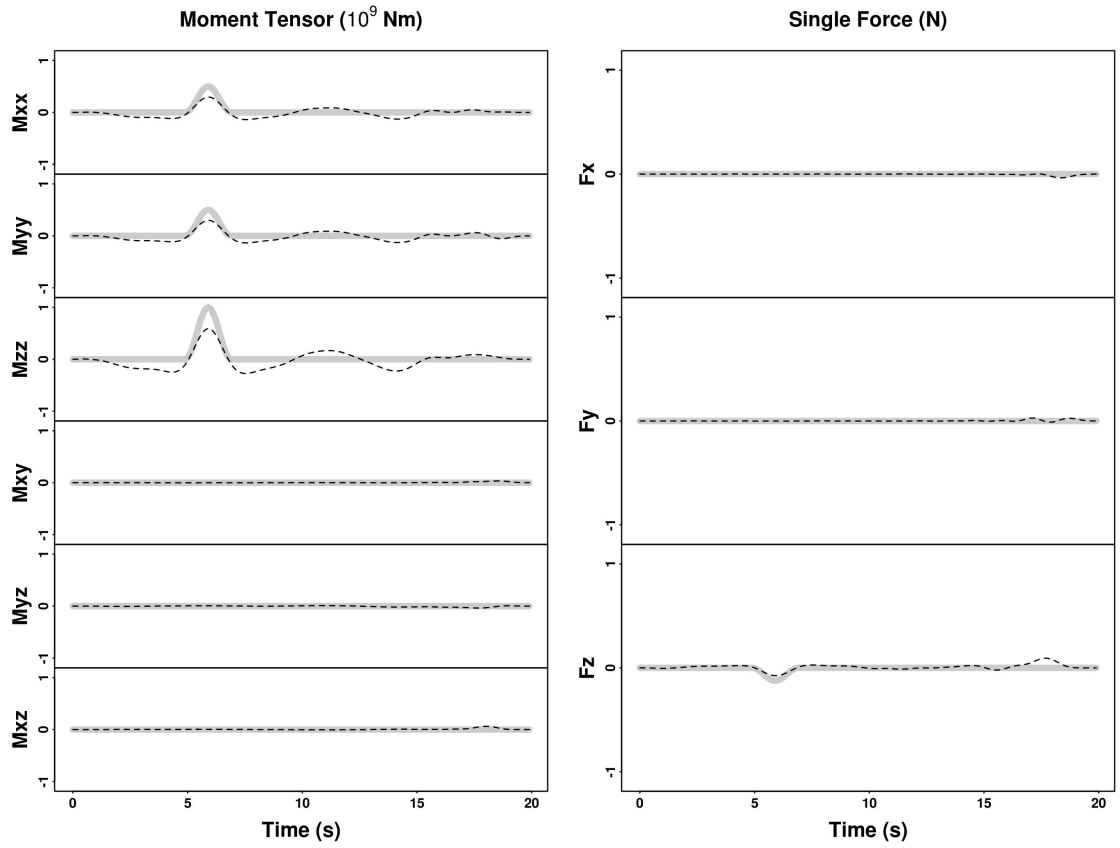

Figure 3.11: Numerical test of the capability of the inversion method to reconstruct known source time functions. The thick solid lines are the original source time functions, and the dot lines indicate the results of the inversion. The ratios of principal dipole components and the single force are $M_{xx} : M_{yy} : M_{zz} = 0.5 : 0.5 : 1$ and F_z/M_{zz} = -0.125 $\times 10^{-3}$ in both time functions, respectively.

single force (F_z) and the vertical dipole (M_{zz}) can be resolved by our station coverage. This synthetic test strongly suggests that the observed downward force is required and physically significant. Since we have eliminated cases 2 and 3, from now on we consider only models of type 1, i.e. models with six moment components and a single force in the vertical dimension.

3.5.4 Source Types

The source time histories of Model 1 are shown in Fig. 3.8. The volumetric components along the main diagonal of the moment tensor clearly dominate. In addition, the vertical dipole, M_{zz}, dominates over the two horizontal dipoles, M_{xx} and M_{yy}. The source mechanism of the source time functions are consistent in time (Fig. 3.9). The directions of the eigenvectors and amplitude ratios of the principal axes of the moment tensor are both stable, indicating that the source mechanism is stationary before and after the peak amplitudes. So, peak-to-peak amplitudes were measured and used as representative values for the time histories of the moment tensor.

Fig. 3.12 shows our resultant moment tensors on a source-type plot (Hudson et al., 1989). The moment tensors are obtained from measurements of the maximum peak-to-peak amplitudes in the individual source time functions and listed in Table 3.2. The source-type plot displays characteristics of the moment tensor in terms of isotropic, double couple (DC), and compensated linear vector dipole (CLVD). In the source-type plot, the general moment tensor are decomposed into an isotropic (volumetric) part and a deviatoric remainder,

$$\begin{bmatrix} M_1 \\ M_2 \\ M_3 \end{bmatrix} = M^{(V)} \begin{bmatrix} 1 \\ 1 \\ 1 \end{bmatrix} + \begin{bmatrix} M_1' \\ M_2' \\ M_3' \end{bmatrix}, \tag{3.6}$$

where $M_{(V)} = (M_1 + M_2 + M_3)/3$. And then we decomposed the deviatoric part into

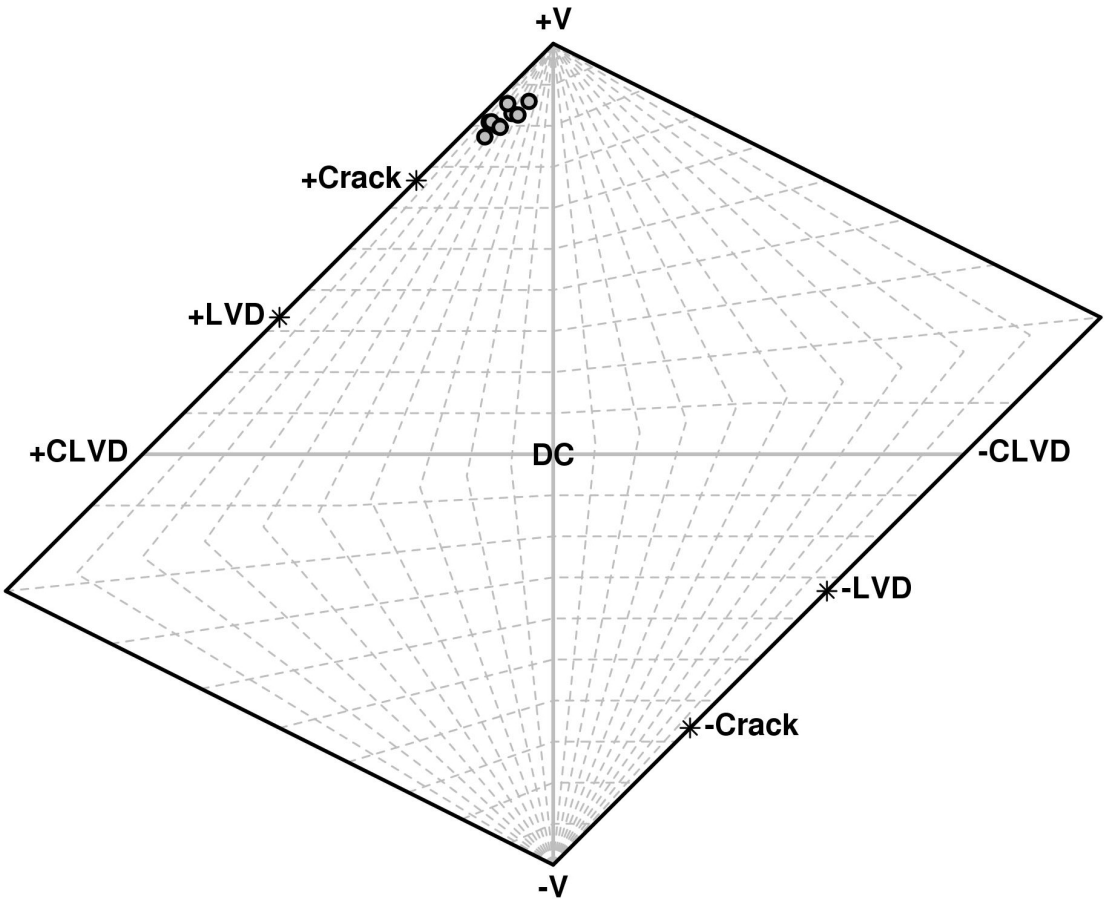

Figure 3.12: Source type plot of Hudson et al. (1989). Source mechanisms for the events are plotted without regard to their orientation. All source mechanisms lie between a pure crack and an isotropic explosion.

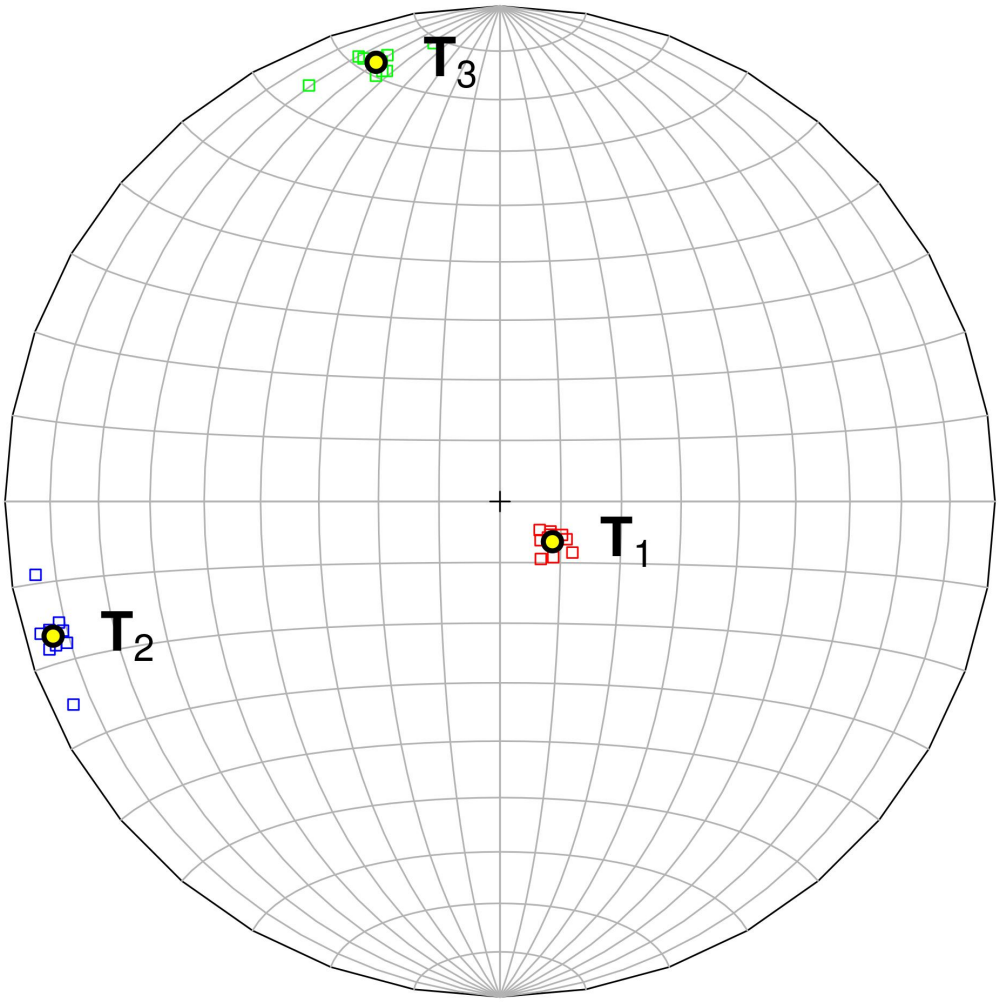

Figure 3.13: The eigenvectors of the moment tensors are projected on the lower hemisphere. The orientation of the three principal axes ($T_1 > T_2 > T_3$) are remarkably consistent through all the events. Mean eigenvectors are denoted by yellow circles.

a DC and a CLVD,

$$\begin{bmatrix} M'_1 \\ M'_2 \\ M'_3 \end{bmatrix} = M^{(DC)} \begin{bmatrix} 0 \\ -1 \\ 1 \end{bmatrix} + M^{(CLVD)} \begin{bmatrix} -\frac{1}{2} \\ -\frac{1}{2} \\ 1 \end{bmatrix}, \tag{3.7}$$

where $M^{(DC)} = M'_1 - M'_2$, and $M^{(CLVD)} = -2M'_1$. The horizontal coordinate of the source-type plot is defined as

$$T = \frac{2M'_1}{M'_3} = -\frac{M^{(CLVD)}}{|M^{(DC)} + M^{(CLVD)}|}, \tag{3.8}$$

which describes the relative sizes of the DC and CLVD components, and the vertical coordinate is

$$k = \frac{M^{(V)}}{|M^V| + |M'_3|}, \tag{3.9}$$

which measures the volume change.

Source mechanisms for all the events involve dominant volume increases ($k = 0.81 \pm 0.02$). Volumetric changes are commonly associated with mass transport in volcanoes and moment tensor inversions including volume changes have been obtained in many studies in volcanic or geothermal areas (Miller et al., 1998; Chouet et al., 2003). The combination of significant CLVD components ($T = -0.67 \pm 0.12$) and volume change probably indicates crack-like focal mechanisms. By assuming Poisson ratio, $\nu = 1/3$, which is appropriate for volcanic rock (Murase and McBIRNEY, 1973), the pure crack mechanism is indicated on the source type plot. While all the events lie somewhere between the pure crack and the isotropic explosion, the observed volume increases are, however, much larger than expected from the pure crack.

The eigenvectors for the moment tensors are plotted in Fig. 3.13. While the eigenvalues are used to obtain source types regardless of directionality of sources, eigenvectors provide the orientation directions of each source type. The orientations

of the three eigenvectors ($T_1 > T_2 > T_3$) for all events are remarkably consistent. Given these observation it would be difficult to explain the large volume increases and the consistent directionality of the source process by a single crack or an isotropic explosion.

Table 3.2: Moment tensor inversion result

No.	Date	Time	M_{xx}^{a}	M_{xy}	M_{xz}	M_{yy}	M_{yz}	M_{zz}	M_0^{b}	m_B^{c}
1	05/29	02:50:01.69	+0.686	+0.018	-0.047	+0.644	+0.037	+0.990	$+1.003 \times 10^{10}$	2.9
2	05/29	11:26:25.79	+0.732	+0.013	-0.039	+0.672	+0.036	+0.991	$+1.208 \times 10^{10}$	2.9
3	05/29	13:49:39.21	+0.738	+0.003	-0.051	+0.702	+0.033	+0.986	$+1.094 \times 10^{10}$	2.9
4	05/30	01:14:18.83	+0.732	+0.016	-0.040	+0.672	+0.031	+0.991	$+1.058 \times 10^{10}$	2.9
5	05/30	03:33:11.70	+0.740	+0.005	-0.047	+0.700	+0.030	+0.989	$+1.204 \times 10^{10}$	2.9
6	05/30	19:16:26.98	+0.781	+0.007	-0.026	+0.715	+0.033	+0.993	$+1.062 \times 10^{10}$	2.9
7	05/31	04:17:29.14	+0.783	+0.016	-0.036	+0.710	+0.049	+0.986	$+5.871 \times 10^{9}$	2.8
8	05/31	08:18:41.83	+0.804	+0.003	-0.042	+0.771	+0.035	+0.986	$+9.094 \times 10^{9}$	2.9
9	06/01	00:50:42.72	+0.827	+0.017	-0.023	+0.761	+0.042	+0.990	$+8.929 \times 10^{9}$	2.9
10	06/01	05:46:17.98	+0.728	+0.019	-0.033	+0.667	+0.029	+0.994	$+5.646 \times 10^{9}$	2.8

[a] All the moment tensor components are normalized with respect to the scalar moment (M_0) event by event.
[b] Scalar moment proposed by Bowers and Hudson (1999)
[c] Body-wave magnitude determined by the relation between m_B and M_0 (Kanamori, 1983)

3.6 Discussion

3.6.1 Geometry of Source Region

A general geometry of source mechanisms can be explained by an arbitrarily oriented tri-axial ellipsoid model (Davis, 1986). In this model, volcanic inflation and deflation is described in terms of a pressurized cavity embedded below the Earth's surface. The ellipsoid orientation is given by the eigenvectors of the moment tensor while the axes of the ellipsoid ($a > b > c$) are inversely related to the moment tensor eigenvalues ($M_3 < M_2 < M_1$). Following Davis (1986), the diagonalized moment tensor, M_{ij}, is defined as

$$M_{ij} = VP_{ij}, \tag{3.10}$$
$$P_{ij} = 0 \qquad \text{if } i \neq j,$$

where V is volume of the ellipsoidal cavity, and P_{ij} is the stress tensor over the cavity. The strain tensor e_{ij} derived from P_{ij} satisfies the following conditions:

$$P_{ij} = \lambda e_{mm}\delta_{ij} + 2\mu e_{ij} \tag{3.11}$$
$$S_{ijkl}e_{kl} - e_{ij} = \frac{\Delta p}{k}\delta_{ij} \tag{3.12}$$

where λ and μ are Lamé constants, Δp is the overpressure over the cavity, and k is the bulk modulus. The S_{ijkl} is given by the three axes ($a > b > c$) of the ellipsoidal cavity (Davis, 1986). Substituting P_{ij} in equation (3.10) with equation (3.11) and

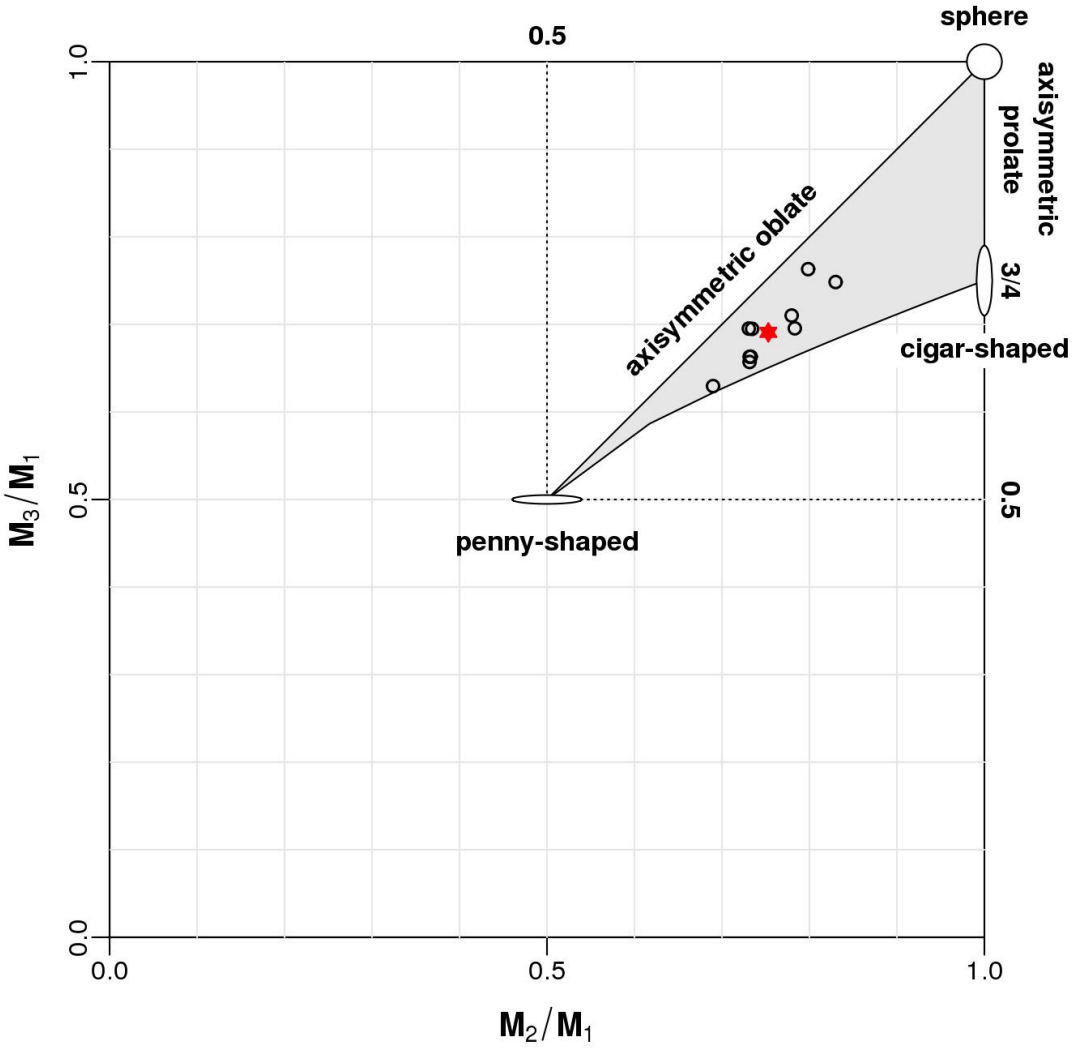

Figure 3.14: Ratios of eigenvalues M_3/M_1 and M_2/M_1. All the events (circle) and mean eigenvalues (star) are plotted by assuming Poisson ratio, $\lambda = 1/3$. All the events are inside the region allowed for ellipsoidal cavities.

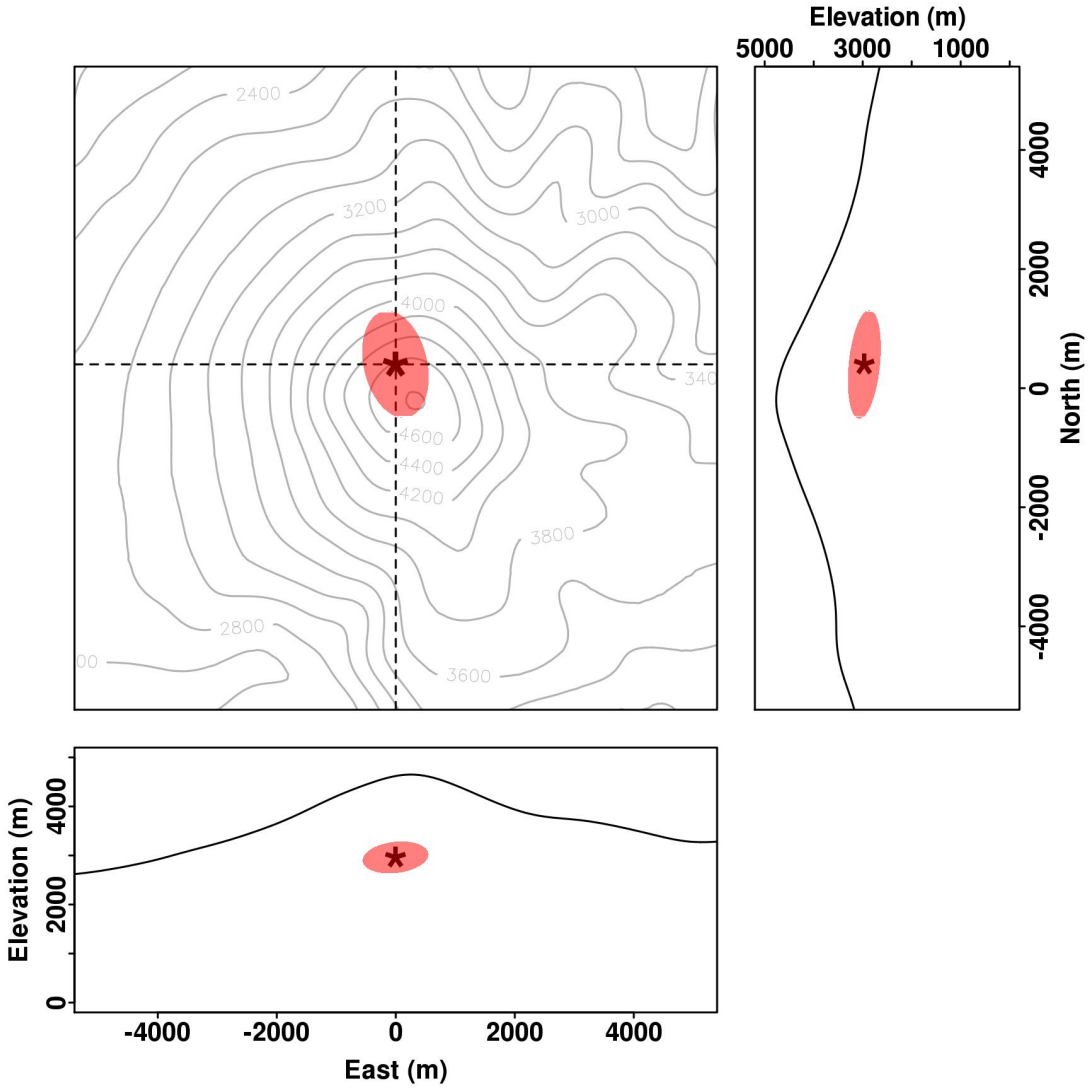

Figure 3.15: Resultant ellipsoidal cavity obtained from the mean eigenvectors. The ellipsoid is centered at the best-fit location. The overall size is arbitrary, depending on choice of V and Δp.

(3.12), the diagonal elements of M_{ij} can be written as

$$\begin{bmatrix} M_{11} \\ M_{22} \\ M_{33} \end{bmatrix} = V\Delta p \frac{\alpha}{\alpha + \frac{2}{3}} \begin{bmatrix} 1+\frac{2}{\alpha} & 1 & 1 \\ 1 & 1+\frac{2}{\alpha} & 1 \\ 1 & 1 & 1+\frac{2}{\alpha} \end{bmatrix} \times \begin{bmatrix} S_{1111}-1 & S_{1122} & S_{1133} \\ S_{2211} & S_{2222}-1 & S_{2233} \\ S_{3311} & S_{3322} & S_{3333}-1 \end{bmatrix}^{-1} \begin{bmatrix} 1 \\ 1 \\ 1 \end{bmatrix}, \tag{3.13}$$

where $\alpha = \lambda/\mu$ ($\alpha = 2$ if $\nu = 1/3$). Only a limited number of eigenvalue ratios (M_{22}/M_{11} vs M_{33}/M_{11}), denoted by the shaded region in Fig. 3.14, will produce ellipsoidal source. Pure crack and isotropic source models are special cases of an ellipsoidal cavity. All events in this study lie inside the shaded boundary in Fig. 3.14, suggesting an ellipsoidal source geometry.

In order to reconstruct a source geometry, we extract the mean eigenvectors from the observed events. The largest mean eigenvector ($\mathbf{T_1}, |\mathbf{T_1}| = M_{11}$) is first estimated from largest eigenvectors of the 10 events (Fig. 3.13). The intermediate mean eigenvector ($\mathbf{T_2}, |\mathbf{T_2}| = M_{22}$) is then computed requiring that it is orthogonal to the first eigenvector. The smallest eigenvector ($\mathbf{T_3}, |\mathbf{T_3}| = M_{33}$) is then obtained by satisfying the orthogonality condition to the first two vectors. Ratios of the mean eigenvector are shown in Fig. 3.14. The ellipsoid orientation is determined from the mean eigenvectors ($\mathbf{T_1}, \mathbf{T_2}, \mathbf{T_3}$), and the axes of the ellipsoid (b/a and c/a) are computed from equation (3.12). The consequent ellipsoidal cavity is shown in Fig. 3.15. As seen by equations, (3.12) and (3.13), unless V or Δp are known, only the relative sizes of the axes can be calculated. If we fix the semi-major axis, a, in the range $100\ m < a < 200\ m$, the cavity volume and the overpressure will vary by $6 \times 10^5\, m^3 < V < 5 \times 10^6\, m^3$ and 1 MPa $> \Delta p >$ 0.1 MPa, respectively.

3.6.2 Time Histories of Source Processes

It is not always clear how processes deep in the volcano edifice relate to observed explosions at the surface of a volcano. To help understand this discrepancy we have made an exhaustive attempt to relate observed seismic waves to acoustic arrival times. Onset times of earthquakes associated with vent explosions at the crater can be compared to investigate the timing of explosive mechanisms. Onset times of the seismic events are defined as the arrival time of the peak amplitude of the moment tensor solutions in the calculated source time histories (Fig. 3.8). Onset times of the explosions are inferred from arrival times of infrasound waves at the five observing stations, assuming a constant sound velocity, using:

$$t_i^o = t_i^a - \frac{d_i}{c}, \tag{3.14}$$

where t_i^o is the origin time derived from the onset of the i^{th} station, d_i is the distance from the summit crater to the i^{th} station, t_i^a is the arrival time at the i^{th} station, and c is the speed of sound in atmosphere. The sound speed is assumed to be 343 m/s, appropriate in air at 20°C. The best fit origin time is selected to minimize the variance of t_i^o among the five stations. We determined origin times for each of the 10 events and the travel time curve is indicated by the dashed line in Fig. 3.16. From this analysis the predicted origin time of infrasonic waves appears to be 0.6 ± 0.3 s earlier than the observed onset times of explosion earthquakes. However, if we assume that shock waves were initially produced by the intense explosions, the wave speeds of the shocks are considerably higher than the acoustic speeds of the infrasonic waves. We can make a simple adjustment and correct the origin times assuming a higher shock wave velocity, and the new infrasound origin times will arrive later than those obtained by assuming a simple, constant acoustic velocity.

Shock waves are commonly observed with Vulcanian explosions. (Ishihara, 1985;

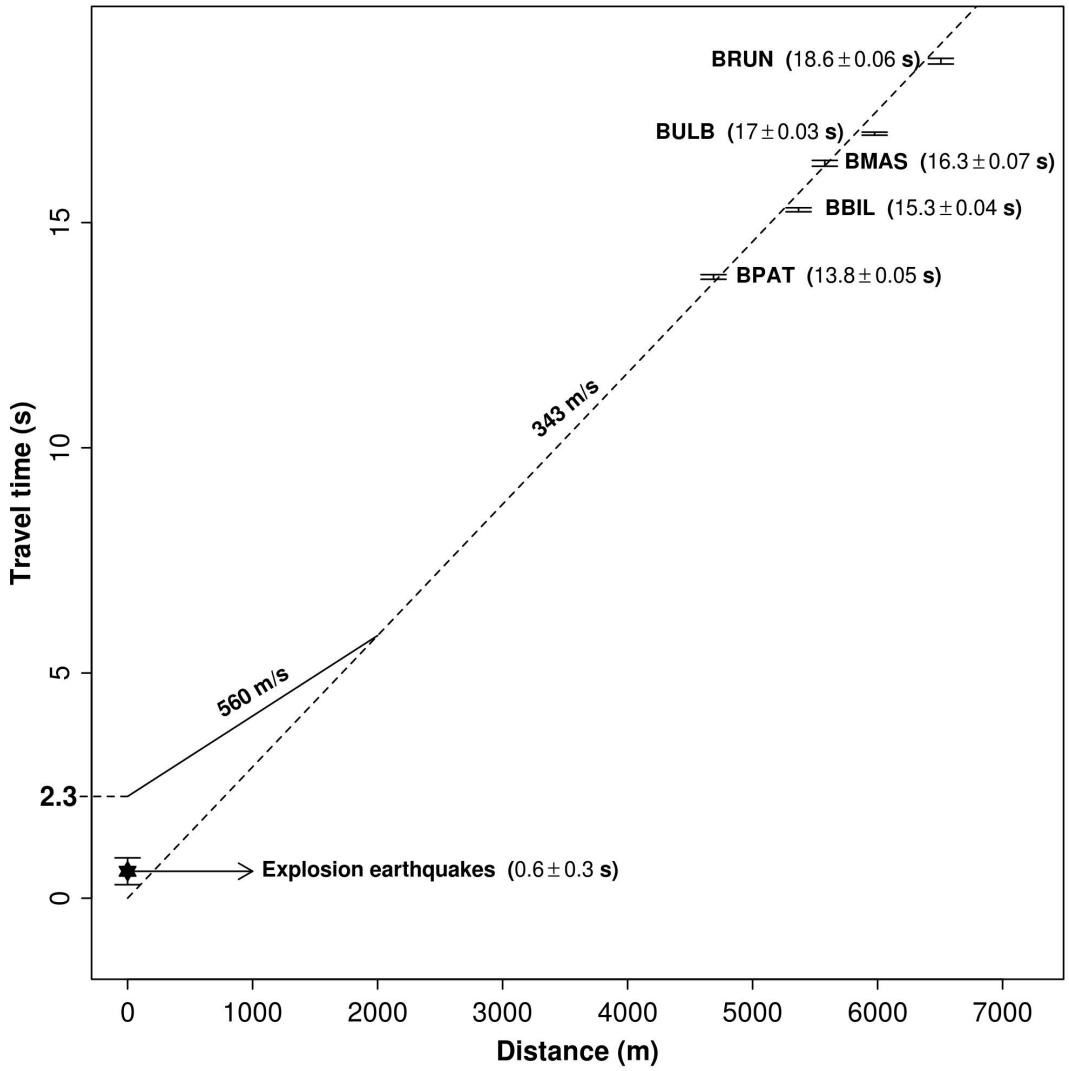

Figure 3.16: Travel time curves for the infrasound excited by the explosion at the crater. The origin times are calculated for the all events by assuming the constant sound speed (343 m/s), and travel times are obtained with respect to the origin times event by event. Mean arrival times and the standard deviations are denoted by stations.

Gottschmmer and Surono, 2000). Shock waves are non-linear waves excited by supersonic flow or very large changes in pressure over short time periods. The higher the overpressure at the shock front, the greater the velocity of the shock wave. Initially, the shock velocity may be quite high, several times the speed of sound in air. As the shock waves propagate away from the vent, the pressure at the shock front decreases and the velocity falls off accordingly, finally approaching the ambient sound speed (Glasstone, 1977). Accordingly, travel time curves for the shock waves are not simply linear and detailed estimates would require dense arrays of sensors located close to the explosion source. Seismic stations at Tungurahua are not optimally positioned to record shock waves. Since they are all located further than 4.8 km from the vent, any shock waves present would have already decreased in speed to the ambient sound velocity. If we adopt a constant shock wave velocity of 560 m/s, e.g. measured at 2 km from the vent of Bromo Volcano, Indonesia (Gottschmmer and Surono, 2000), surface explosions at Tungurahua would have occurred 1.7 ± 0.3 seconds later than the associated explosion earthquakes (Fig. 3.16).

This seems to agree better with our preconceived notion of the ordering of surface versus deep conduit events. While the origin time of infrasound suggests that explosion earthquakes should occur in time near the onset of surface explosions, the time sequence of these two events remains ambiguous, and probably depends on the importance of shock waves in the propagation of these signals. In the following we will therefore interpret the source time history by considering two exclusive scenarios:

1. Deep seismic source are triggered by the explosions at the crater.
2. Deep seismic sources trigger surface explosions.

Kanamori et al. (1984) proposed a seismic source model of explosive eruptions following the first hypothesis. They suggested that the sudden removal of the cap above a pressurized magma cavity, at shallow depth, causes an volcanic explosion. The explosion can be represented by a combination of a downward vertical force and

an implosive moment tensor. The downward vertical force is a reaction force to the volcanic jet or volcanic ejecta. The implosive moment tensor produces pressure decreases of the shallow magma reservoir as volcanic gases are released. Many volcanic eruptions associated with significant deflation have been interpreted using this model (Kanamori et al., 1984; Uhira and Takeo, 1994; Nishimura, 1998; Ohminato, 2006). If Tungurahua explosion earthquakes were triggered by surface explosions, they should have shown significant surface deformation in the form of deflation. However, the first observed P-wave motions were compressional at all stations, indicating an inflation process. According to this model, surface eruptions are associated with shallow ($<$ 1 Km) explosion earthquakes. Tungurahua explosion earthquakes are evidently too deep (1.6 km below the crater) to be coupled simultaneously to surface explosions. Given this discrepancy, we may exclude scenario 1 and accept the alternative, suggesting that the deeper events control the shallow activity. In scenario 2, explosion earthquakes can be interpreted by a model initially proposed by Tameguri et al. (2002). The authors suggest that explosive eruptions are triggered by pressure waves initiated via a deep source. Tameguri et al. (2002) observed an explosive earthquake preceding an associated surface eruption at Mt. Sakurajima, and showed that it was generated by isotropic expansion at a depth of 2 km. Deep explosive earthquakes preceding eruptions at Sakurajima, Suwanosejima, and Semeru volcanoes were also observed by Ishihara (1985) and Iguchi et al. (2008). Moment tensor analysis of Tungurahua explosion earthquakes indicate abrupt pressure fluctuations in a sill-shaped subsurface crack or cavity, 1.6 km below the summit. According to this model (Tameguri et al., 2002), the pressure wave induced by the seismic fluctuations in the conduit or magma cavity propagates upward, along the conduit towards the crater, finally triggering the surface explosion. The initial pressure disturbance may be caused by a sudden degassing, an influx of material or the collapse of a gas pocket. The burst of the gas pocket possibly opens a pathway for gases to propagate and

escape, forcing flow and causing a pressure drop in the deep source region (Uhira and Takeo, 1994). An upward gas flux may explain the downward single force that coincides with the inflation in the derived moment tensor solutions (Fig. 3.8). A single force on the Earth can be generated by an exchange of linear momentum between the source volume and the surrounding region (Chouet et al., 2005). The overpressured gas and magma should be forced into the vertical conduit that connects the magma-gas cavity and the surface crater, and the resultant upward acceleration is physically represented by a single downward oriented force. Comparing these two alternative scenarios, the violent explosions at the summit crater of Tungurahua in 2010 appear to be best explained by the triggering effect of deep explosion earthquakes.

3.7 Conclusion

In this chapter we investigate source mechanisms of Vulcanian explosions at Tungurahua volcano. Low-frequency seismic events associated with explosive eruptions were inverted to derive source models including moment tensors and single forces. The calculated inversion results suggest a seismic source 1.6 km below and 400 m north of the summit crater. The moment tensor solutions are best represented by a single ellipsoidal pressurized cavity or crack. The semi-minor axis of the ellipsoid is nearly vertical, indicating a horizontal, or sill-like cavity. The overpressure in the source region is estimated to be in the range 1 MPa - 0.1 MPa, if the semi-major axis ranges 100 m - 200 m. The onset time of the surface explosion and the source time histories of the moment tensors suggest that surface explosions were triggered by deeper seismic events. Abrupt pressure increases and decreases at the deep source region may be caused by the burst of gas pocket or bubble. The bursting or collapsing gas bubble subsequently opens a pathway for gases to escape and followed by the triggered surface explosion. The downward single force in our solution may be produced

by an exchange of linear momentum between the source and the surrounding region during the escaping gas flow.

References

Akaike, H. (1974). A new look at the statistical model identification. *Automatic Control, IEEE Transactions on*, 19(6):716 – 723.

Aster, R., Zandomeneghi, D., Mah, S., McNamara, S., Henderson, D., Knox, H., and Jones, K. (2008). Moment tensor inversion of very long period seismic signals from Strombolian eruptions of Erebus Volcano. *Journal of Volcanology and Geothermal Research*, 177(3):635 – 647.

Auger, E., D'Auria, L., Martini, M., Chouet, B., and Dawson, P. (2006). Real-time monitoring and massive inversion of source parameters of very long period seismic signals: An application to Stromboli Volcano, Italy. *Geophysical Research Letters*, 33(4):L04301.

Berenger, J. (1994). A perfectly matched layer for the absorption of electromagnetic waves. *Journal of Computational Physics*, 114(2):185–200.

Bouche, E., Vergniolle, S., Staudacher, T., Nercessian, A., Delmont, J.-C., Frogneux, M., Cartault, F., and Pichon, A. L. (2010). The role of large bubbles detected from acoustic measurements on the dynamics of Erta 'Ale lava lake (Ethiopia). *Earth and Planetary Science Letters*, 295(12):37 – 48.

Bowers, D. and Hudson, J. A. (1999). Defining the scalar moment of a seismic source with a general moment tensor. *Bulletin of the Seismological Society of America*, 89(5):1390–1394.

Cannata, A., Hellweg, M., Grazia, G. D., Ford, S., Alparone, S., Gresta, S., Montalto, P., and Patan, D. (2009). Long period and very long period events at Mt. Etna Volcano: Characteristics, variability and causality, and implications for their sources. *Journal of Volcanology and Geothermal Research*, 187(34):227 – 249.

Caplan-Auerbach, J., Bellesiles, A., and Fernandes, J. K. (2010). Estimates of eruption velocity and plume height from infrasonic recordings of the 2006 eruption of Augustine Volcano, Alaska. *Journal of Volcanology and Geothermal Research*, 189(1-2):12 – 18.

Cheney, E. and Kincaid, D. (2007). *Numerical Mathematics and Computing*. Brooks/Cole Pub Co., Pacific Grove, CA.

Chouet, B. (1996). New methods and future trends in seismological volcano monitoring. *Monitoring and Mitigation of Volcano Hazards*, pages 23–97.

Chouet, B. and Dawson, P. (2011). Shallow conduit system at Kilauea Volcano, Hawaii, revealed by seismic signals associated with degassing bursts. *Journal of Geophysical Research*, 116(B12):B12317.

Chouet, B., Dawson, P., and Arciniega-Ceballos, A. (2005). Source mechanism of vulcanian degassing at Popocatépetl Volcano, Mexico, determined from waveform inversions of very long period signals. *Journal of Geophysical Research*, 110(B7):B07301.

Chouet, B., Dawson, P., Ohminato, T., Martini, M., Saccorotti, G., Giudicepietro, F., De Luca, G., Milana, G., and Scarpa, R. (2003). Source mechanisms of explosions at Stromboli volcano, Italy, determined from moment-tensor inversions of very-long-period data. *Journal of Geophysical Research*, 108(B7):2331.

Chouet, B. A., Dawson, P. B., James, M. R., and Lane, S. J. (2010). Seismic source mechanism of degassing bursts at Kilauea Volcano, Hawaii: Results from waveform inversion in the 10-50 s band. *Journal of Geophysical Research*, 115(B9):B09311.

Curle, N. (1955). The influence of solid boundaries upon aerodynamic sound. *Proceedings of the Royal Society of London. Series A, Mathematical and Physical Sciences*, 231(1187):pp. 505–514.

Davis, P. M. (1986). Surface deformation due to inflation of an arbitrarily oriented triaxial ellipsoidal cavity in an elastic half-space, with reference to Kilauea Volcano, Hawaii. *Journal of Geophysical Research: Solid Earth*, 91(B7):7429–7438.

Dawson, P. B., Chouet, B. A., and Power, J. (2011). Determining the seismic source mechanism and location for an explosive eruption with limited observational data: Augustine Volcano, Alaska. *Geophysical Research Letters*, 38(3):L03302.

de Groot-Hedlin, C. (2008). Finite-difference time-domain synthesis of infrasound propagation through an absorbing atmosphere. *The Journal of the Acoustical Society of America*, 124(3):1430–1441.

Fee, D., Garces, M., and Steffke, A. (2010). Infrasound from Tungurahua Volcano 2006-2008: Strombolian to Plinian eruptive activity. *Journal of Volcanology and Geothermal Research*, 193(1-2):67 – 81.

Garces, M. A. and McNutt, S. R. (1997). Theory of the airborne sound field generated in a resonant magma conduit. *Journal of Volcanology and Geothermal Research*, 78(3-4):155–178.

Glasstone, S. (1977). *The Effects of Nuclear Weapons*. U.S. Gov. Print. Off., Washington, D.C., 1977.

Gottschmmer, E. and Surono, I. (2000). Locating tremor and shock sources recorded at Bromo Volcano. *Journal of Volcanology and Geothermal Research*, 101(12):199 – 209.

Harris, G. (1981). Review of transient field theory for a baffled planar piston. *The Journal of the Acoustical Society of America*, 70(1):10.

Hudson, J. A., Pearce, R. G., and Rogers, R. M. (1989). Source type plot for inversion of the moment tensor. *Journal of Geophysical Research*, 94(B1):765–774.

Iguchi, M., Yakiwara, H., Tameguri, T., Hendrasto, M., and Hirabayashi, J. (2008). Mechanism of explosive eruption revealed by geophysical observations at the Sakurajima, Suwanosejima and Semeru Volcanoes. *Journal of Volcanology and Geothermal Research*, 178(1):1 – 9.

Ishihara, K. (1985). Dynamical analysis of volcanic explosion. *Journal of Geodynamics*, 3(34):327 – 349.

Jackson, D. D. (1972). Interpretation of inaccurate, insufficient and inconsistent data. *Geophysical Journal of the Royal Astronomical Society*, 28(2):97–109.

Johnson, J. (2003). Generation and propagation of infrasonic airwaves from volcanic explosions. *Journal of Volcanology and Geothermal Research*, 121(1-2):1–14.

Johnson, J. (2007). On the relation between infrasound, seismicity, and small pyroclastic explosions at Karymsky Volcano. *Journal of Geophysical Research*, 112:B08203.

Johnson, J. and Aster, R. (2005). Relative partitioning of acoustic and seismic energy during Strombolian eruptions. *Journal of Volcanology and Geothermal Research*, 148(3-4):334–354.

Johnson, J., Aster, R., Jones, K., Kyle, P., and McIntosh, B. (2008). Acoustic source characterization of impulsive strombolian eruptions from the Mount Erebus lava lake. *Journal of Volcanology and Geothermal Research*, 177(3):673–686.

Johnson, J., Aster, R., Ruiz, M., Malone, S., McChesney, P., Lees, J., and Kyle, P. (2003). Interpretation and utility of infrasonic records from erupting volcanoes. *Journal of Volcanology and Geothermal Research*, 121(1-2):15–63.

Johnson, J., Lees, J., and Yepes, H. (2006). Volcanic eruptions, lightning, and a waterfall: Differentiating the menagerie of infrasound in the Ecuadorian jungle. *Geophysical Research Letters*, 33(6):L06308.

Johnson, J. B., Aster, R. C., and Kyle, P. R. (2004). Volcanic eruptions observed with infrasound. *Geophysical Research Letters*, 31(14):L14604.

Johnson, J. B. and Lees, J. M. (2010). Sound produced by the rapidly inflating Santiaguito lava dome, Guatemala. *Geophysical Research Letters*, 37:L22305.

Kanamori, H. (1983). Magnitude scale and quantification of earthquakes. *Tectonophysics*, 93(34):185 – 199.

Kanamori, H., Given, J. W., and Lay, T. (1984). Analysis of seismic body waves excited by the Mount St. Helens eruption of may 18, 1980. *Journal of Geophysical Research*, 89(B3):1856–1866.

Kanamori, H., Mori, J., and Harkrider, D. (1994). Excitation of atmospheric oscillations by volcanic eruptions. *Journal of Geophysical Research*, 99:21947–21961.

Kim, K. and Lees, J. M. (2011). Finite-difference time-domain modeling of transient infrasonic wavefields excited by volcanic explosions. *Geophysical Research Letters*, 38(6):L06804.

Kim, K., Lees, J. M., and Ruiz, M. (2012). Acoustic multipole source model for volcanic explosions and inversion for source parameters. *Geophysical Journal International*, 191(3):1192–1204.

Kumagai, H., Chouet, B., and Dawson, P. (2005). Source process of a long-period event at Kilauea Volcano, Hawaii. *Geophysical Journal International*, 161(1):243–254.

Kumagai, H., Placios, P., Ruiz, M., Yepes, H., and Kozono, T. (2011). Ascending seismic source during an explosive eruption at Tungurahua Volcano, Ecuador. *Geophysical Research Letters*, 38(1):L01306.

Leehey, P. and Hanson, C. (1970). Aeolian tones associated with resonant vibration. *Journal of Sound and Vibration*, 13(4):465 – 483.

Lees, J., Gordeev, E., and Ripepe, M. (2004). Explosions and periodic tremor at Karymsky Volcano, Kamchatka, Russia. *Geophysical Journal International*, 158(3):1151–1167.

Li, K. M., Taherzadeh, S., and Attenborough, K. (1997). Sound propagation from a dipole source near an impedance plane. *The Journal of the Acoustical Society of America*, 101(6):3343–3352.

Lighthill, M. J. (1952). On sound generated aerodynamically. i. general theory. *Proceedings of the Royal Society of London. Series A, Mathematical and Physical Sciences*, 211(1107):564–587.

Lighthill, M. J. (1978). *Waves in Fluids*. Cambridge University Press, New York, NY

Liu, Q. (1999). Perfectly matched layers for elastic waves in cylindrical and spherical coordinates. *The Journal of the Acoustical Society of America*, 105:2075.

Matoza, R. S., Fee, D., Garcs, M. A., Seiner, J. M., Ramn, P. A., and Hedlin, M. A. H. (2009). Infrasonic jet noise from volcanic eruptions. *Geophysical Research Letters*, 36(8):L08303.

Miller, A. D., Foulger, G. R., and Julian, B. R. (1998). Non-double-couple earthquakes 2. observations. *Reviews of Geophysics*, 36(4):551–568.

Molina, I., Kumagai, H., Pennec, J.-L. L., and Hall, M. (2005). Three-dimensional p-wave velocity structure of Tungurahua Volcano, Ecuador. *Journal of Volcanology and Geothermal Research*, 147(1-2):144 – 156.

Moran, S. C., Matoza, R. S., Garcs, M. A., Hedlin, M. A. H., Bowers, D., Scott, W. E., Sherrod, D. R., and Vallance, J. W. (2008). Seismic and acoustic recordings of an unusually large rockfall at Mount St. Helens, Washington. *Geophysical Research Letters*, 35(19):L19302.

Morse, P. and Ingard, K. (1986). *Theoretical Acoustics*. Princeton University Press, Princeton, NJ.

Murase, T. and McBirney, A. (1973). Properties of some common igneous rocks and their melts at high temperatures. *Geological Society of America Bulletin*, 84(11):3563.

Nishimura, T. (1998). Source mechanisms of volcanic explosion earthquakes: single force and implosive sources. *Journal of Volcanology and Geothermal Research*, 86(14):97 – 106.

Ohminato, T. (2006). Characteristics and source modeling of broadband seismic signals associated with the hydrothermal system at Satsuma-Iwojima Volcano, Japan. *Journal of Volcanology and Geothermal Research*, 158(3-4):467 – 490.

Ohminato, T. and Chouet, B. A. (1997). A free-surface boundary condition for including 3D topography in the finite-difference method. *Bulletin of the Seismological Society of America*, 87(2):494–515.

Ohminato, T., Chouet, B. A., Dawson, P., and Kedar, S. (1998). Waveform inversion of very long period impulsive signals associated with magmatic injection beneath Kilauea Volcano, Hawaii. *Journal of Geophysical Research*, 103(B10):23839–23862.

Ohminato, T., Takeo, M., Kumagai, H., Yamashina, T., Oikawa, J., Koyama, E., Tsuji, H., and Urabe, T. (2006). Vulcanian eruptions with dominant single force components observed during the Asama 2004 volcanic activity in Japan. *Earth Planets and Space*, 58(5):583.

Ostashev, V., Wilson, D., Liu, L., Aldridge, D., Symons, N., and Marlin, D. (2005). Equations for finite-difference, time-domain simulation of sound propagation in moving inhomogeneous media and numerical implementation. *The Journal of the Acoustical Society of America*, 117:503.

Ozerov, A., Ispolatov, I., and Lees, J. (2003). Modeling Strombolian eruptions of Karymsky Volcano, Kamchatka, Russia. *Journal of Volcanology and Geothermal Research*, 122(3-4):265–280.

Parker, R. (1994). *Geophysical Inverse Theory*. Princeton University Press, Princeton, NJ.

Pierce, A. (1989). *Acoustics: An Introduction to its Physical Principles and Applications*. Acoustical Society of America, Woodbury, NY

Ripepe, M., Marchetti, E., and Ulivieri, G. (2007). Infrasonic monitoring at Stromboli Volcano during the 2003 effusive eruption: Insights on the explosive and degassing process of an open conduit system. *Journal of Geophysical Research*, 112(B9):B09207.

Rossing, T. (2007). *Springer Handbook of Acoustics*. Springer Verlag, New York, NY.

Ruiz, M., Lees, J., and Johnson, J. (2006). Source constraints of Tungurahua Volcano explosion events. *Bulletin of Volcanology*, 68(5):480–490.

Sparks, R. S. J. (1997). *Volcanic Plumes*. Wiley, New York.

Stump, B. W. and Johnson, L. R. (1977). The determination of source properties by the linear inversion of seismograms. *Bulletin of the Seismological Society of America*, 67(6):1489–1502.

Sutherland, L. C. and Bass, H. E. (2004). Atmospheric absorption in the atmosphere up to 160 km. *The Journal of the Acoustical Society of America*, 115(3):1012–1032.

Tameguri, T., Iguchi, M., and Ishihara, K. (2002). Mechanism of explosive eruptions from moment tensor analyses of explosion earthquakes at Sakurajima Volcano, Japan. *Bulletin of the Volcanological Society of Japan*, 47(4):197–215.

Uhira, K. and Takeo, M. (1994). The source of explosive eruptions of Sakurajima Volcano, Japan. *Journal of Geophysical Research*, 99(B9).

Vergniolle, S., Boichu, M., and Caplan-Auerbach, J. (2004). Acoustic measurements of the 1999 basaltic eruption of Shishaldin Volcano, Alaska 1. origin of Strombolian activity. *Journal of Volcanology and Geothermal Research*, 137(1-3):109–134.

Vergniolle, S. and Brandeis, G. (1994). Origin of the sound generated by Strombolian explosions. *Geophysical Research Letters*, 21(18):1959–1962.

Vergniolle, S., Brandeis, G., and Mareschal, J. (1996). Strombolian explosions 2. eruption dynamics determined from acoustic measurements. *Journal of Geophysical Research*, 101(B9):20,449–20,466.

Vergniolle, S. and Caplan-Auerbach, J. (2004). Acoustic measurements of the 1999 basaltic eruption of Shishaldin Volcano, Alaska: 2. precursor to the Subplinian phase. *Journal of Volcanology and Geothermal Research*, 137(1-3):135 – 151.

Vergniolle, S. and Caplan-Auerbach, J. (2006). Basaltic thermals and Subplinian plumes: Constraints from acoustic measurements at Shishaldin Volcano, Alaska. *Bulletin of Volcanology*, 68:611–630.

Wang, S. (1996). Finite-difference time-domain approach to underwater acoustic scattering problems. *The Journal of the Acoustical Society of America*, 99(4):1924–1931.

Weight, J. P. and Hayman, A. J. (1978). Observations of the propagation of very short ultrasonic pulses and their reflection by small targets. *The Journal of the Acoustical Society of America*, 63(2):396–404.

Wilson, C. and Forbes, R. (1969). Infrasonic waves from Alaskan volcanic eruptions. *Journal of Geophysical Research*, 74(18):4511–4522.

Woulff, G. and McGetchin, T. R. (1976). Acoustic noise from volcanoes: Theory and experiment. *Geophysical Journal of the Royal Astronomical Society*, 45:601–616.

Yee, K. (1966). Numerical solution of initial boundary value problems involving maxwell's equations in isotropic media. *IEEE Transactions on Antennas and Propagation*, 14(3):302–307.